Surveys in Geophysics manuscript No.
(will be inserted by the editor)

Artifacts in high-frequency surface wave dispersion imaging

– Towards the linear receiver array

Feng Cheng · Jianghai Xia

Received: Jun, 2021 / Accepted: XX, XXXX

Abstract Surface wave methods are non-invasive, low-cost, and robust approaches to image near-surface S-wave velocity (Vs) structure. In terms of the energy source types, they can be classified into two groups: active-source surface wave methods and passive-source surface wave methods. A clean and high-resolution dispersion image is critical for dispersion curve picking as well as Vs inversion in surface wave analysis. In practice, however, aliasing or other artifacts are almost inevitable in surface wave dispersion measurements , and they can seriously pollute the true dispersion spectra. It is significant to figure out how they are generated, how they affect the dispersion measurement, and how they can be attenuated. We provide the first comprehensive review on artifacts that are frequently observed in surface wave dispersion measurements, and summarize them into three general types, including artifacts from sparse spatial sampling, array response artifacts, and artifacts from low signal coherency. Both numerical and field examples, as well as mathematical derivations, are presented to help the reader understand the source of the various types artifacts and the way to attenuate them. This work will help the reader understand the complexity of the measured dispersion spectra, and lead to potential improvements on surface wave dispersion analysis.

Keywords Surface wave · Passive-source · Active-source · Dispersion measurement · Aliasing · Artifacts

F. Cheng
[1]Dept. of Earth, Environmental, and Planetary Sciences
Rice University
6100 Main St., Houston, TX 77005, USA
[2]Lawrence Berkeley National Laboratory
1 Cyclotron Rd., Berkeley, CA, 94720, USA
E-mail: marscfeng@rice.edu

J. Xia
School of Earth Sciences
Zhejiang University
38 Zheda Rd., Hangzhou, Zhejiang 310027, China
E-mail: jhxia@zju.edu.cn

1 Introduction

Surface waves are guided and dispersive. Shear (S)-wave velocity structure can be determined by inverting the dispersive phase velocity of surface waves (Dorman and Ewing, 1962), due to the high sensitivity of dispersion curves to S-wave velocity(Xia et al., 1999). With advantages of cost, acquisition time, and robustness in a variety of contexts, surface wave methods, particularly techniques based on analysis of Rayleigh waves, have been widely utilized at multiple scales in both engineering and classical geological studies (Miller et al., 1999; Xia et al., 1999, 2009; Socco et al., 2010; Nakata et al., 2011; Foti et al., 2018). They can be classified into two groups associated with the energy source type: active-source surface wave methods and passive-source surface wave methods.

Active-source surface wave methods usually use sledgehammers (Park et al., 1999), weight drops (Xia et al., 2000), or vibrators (Miller et al., 1999) as seismic sources. Stokoe and Nazarian (1983) and Nazarian et al. (1983) present the SASW method (spectral analysis of surface waves) to analyze the dispersion curve of Rayleigh waves for near-surface S-wave velocities characterization. To improve inherent difficulties in evaluating and distinguishing signal from noise with only one pair of receivers in SASW measurements, the multichannel analysis of surface wave (MASW) method, using multiple geophones (i.e., 12–24), was developed (Song et al., 1989; Miller et al., 1999; Park et al., 1999; Xia et al., 1999, 2003, 2009; Socco et al., 2010; Park and Carnevale, 2010; Pan et al., 2019). With the development of horizontal excitation sources as well as the multiple component instruments, multichannel analysis of Love wave (MALW) also draws more and more attentions (Song et al., 1989; Winsborrow et al., 2003; Safani et al., 2005; Zeng et al., 2007; Eslick et al., 2008; Xia et al., 2012; Yin et al., 2014; Pan et al., 2016a; Mi et al., 2018, 2020). Compared to MASW, MALW usually benefits from simpler and cleaner dispersion measurements, because Love waves are independent of P wave velocity (Xia et al., 2012). A key step in MASW, as well as MALW, is to generate reliable and high-resolution dispersion spectra; accurate dispersion curves can then be manually or automatically picked by following peaks of dispersion spectra along with different frequencies and finally inverted for 1D Vs profiles. Several techniques are available for surface wave dispersion spectra calculation: the $\tau - p$ transformation (McMechan and Yedlin, 1981), the $f - k$ transformation (Yilmaz, 1987, p.430), the phase-shift method (Park et al., 1998), the frequency decomposition and slant stacking method (Xia et al., 2007), and the high-resolution linear Radon transformation (HLRT, Luo et al., 2008).

The passive-source surface wave methods use ambient seismic energy from natural or anthropogenic sources (e.g., small earthquakes (Poupinet et al., 1984), ocean-seafloor interaction (Lepore and Grad, 2020), traffic (Nakata et al., 2011), and industrial activities (Pan et al., 2016b)). Passive-source surface wave methods have flourished over the past two decades in the geophysical and civil engineering communities because of the logistical challenges and costs from traditional seismic surveys, particularly in highly populated urban areas. The first passive-source surface wave study originated over 60 years ago in pioneering works by Aki (1957, 1965), which is known as the spatial autocorrelation (SPAC) method. Okada and Suto (2003) offers a comprehensive review of the SPAC method and further extended the SPAC method using microtremor array measurement (MAM) to improve the flexibility of the receiver configuration and the investigation depth of the objective structure. Aki's work has been revisited in light of advances of ambient noise interferometry technique following the groundbreaking work of Campillo and Paul (2003). Ambient noise interferometry estimates Green's functions between cross-correlation of two receivers from the ambient seismic field (Shapiro and Campillo, 2004; Snieder, 2004; Wapenaar, 2004; Bensen et al., 2007; Snieder et al., 2009; Nakata et al., 2015). This approach has been applied to characterize multiple scales of earth structure: from global or continental scale deep-structure imaging in seismology (e.g., Yang et al., 2007; Lin et al., 2008; Yao and van der Hilst, 2009; Lin et al., 2009; Strobbia and Cassiani, 2011) to local scale exploration (e.g., Bakulin and Calvert, 2006; Wapenaar et al., 2008; Draganov et al., 2009; Nakata et al., 2011; Ali et al., 2013; Behm et al., 2014; Nakata et al., 2016; Castellanos et al., 2020). During the last decade, ambient noise interferometry has also found a variety of applications in the near-surface characterization domain (e.g., Foti et al., 2011; O'Connell and Turner, 2011; Xu et al., 2013; Cheng et al., 2015; Foti et al., 2018; Dou et al., 2017; Cheng et al., 2018a). Since ambient noise interferometry technique turns the physical receivers into virtual sources, it offers the potential to apply active-source seismic methods on passive-source seismic data. Cheng et al. (2016) provide a method by combining ambient noise interferometry and multichannel analysis of surface wave for passive-source surface wave dispersion imaging, called multichannel analysis of passive surface waves (MAPS).

Apart from the interferometry-based methods, several passive-source surface wave approaches have already existed and been popular in the seismic engineering communities in the early 2000s. Louie (2001) presented the refraction microtremor (ReMi) method as a fast and effective passive-source surface wave imaging method based on the $\tau-p$ transformation, or slant-stacking (Thorson and Claerbout, 1985). Park et al. (2004) introduced a similar strategy for dispersion imaging of passive-source surface waves using the phase-shift method, called passive multichannel analysis of surface wave (PMASW). Besides, two-dimensional (2D) array based method, frequency-wavenumber (f-k) analysis (Capon, 1969a; Lacoss et al., 1969), has also been revisited and extended for 1D linear array application (Liu et al., 2020).

Based on the data processing schemes, the above mentioned passive-source surface wave methods can be roughly divided into two groups: non-interferometric methods (e.g., ReMi and PMASW) and interferometric methods (e.g., MAPS and SPAC). Non-interferometric methods directly extract dispersion measurements from ambient seismic records (Louie, 2001; Park et al., 2004), while interferometric methods calculate interferograms before dispersion measurements is applied, where interferograms are either empirical Green's function (Le Feuvre et al., 2015; Cheng et al., 2016) or spatial autocorrelation coefficients (also known as spatially averaged coherency (Asten, 2006; Chávez-García et al., 2006)). Several studies have explicitly provided the equivalent relationship between Green's functions (or cross-correlation functions) and spatial autocorrelation functions (Asten, 2006; Nakahara, 2006; Tsai and Moschetti, 2010; Haney et al., 2012). However, recent works have argued that interferometric methods have advantages over non-interferometric methods (Cheng et al., 2016; Xu et al., 2017). Cheng et al. (2020) provided comprehensive comparisons between non-interferometric and interferometric passive-source surface wave imaging methods, and concluded that the interferometric methods offer more accurate dispersion imaging in terms of the linear acquisition system.

Irregardless of active or passive sources, a clean and high-resolution dispersion image without aliasing or artifacts is critical for dispersion curve picking and the subsequent Vs inversion. Compared with the active-source methods, the passive-source methods have the advantage of extending the investigation depth due to the broader bandwidth from abundant passive sources, particularly at lower frequencies. Since the temporal and spatial distribution of ambient noise sources are unexpected, however, the passive-source methods are more prone to incoherent noise, particularly at higher frequencies (Cheng et al., 2018b, 2019). Aliasing or artifacts are almost inevitable for either active-source or passive-source surface wave surveys, although the former can usually provide much better dispersion measurements. Several studies have attempted to improve surface wave dispersion measurements, for example, enhancing dispersion imaging resolution (Luo et al., 2008; Mikesell et al., 2017), deblurring of surface wave dispersion spectra (Picozzi et al., 2010; Cheng et al., 2021b), analyzing and filtering surface wave energy (Park et al., 2002; Ivanov et al., 2005), and selectively stacking noise segments for passive-source surface wave dispersion imaging (Cheng et al., 2018b, 2019; Pang et al., 2019). Only a few studies were devoted to investigate the sources of the aliasing or artifacts, and how to attenuate them. Turner (1990) presented the aliasing problems in the $\tau - p$ transform due to the insufficient spatial sampling. Cheng et al. (2018b) first discussed a kind of "crossed" artifacts for high-frequency passive-source surface wave surveys, explaining the underlying physics and proposed an effective way to attenuate them by using FK-based data selection. Dai et al. (2018) discussed the effects of aliasing on wavefield decomposition.

In this work, we seek to provide a comprehensive review on artifacts that are frequently observed in surface wave dispersion measurements, and explore how they are generated and how to eliminate them. The current paper is organized as follows. We first reviewed the existing surface wave methods, including both active-source and passive-source methods, from the data processing workflow to the mathematical derivations of the dispersion imaging scheme. Next, we summarized three types of artifacts, including artifacts from sparse spatial sampling, array response artifacts and artifacts from weak coherent signals. Both numerical examples and field examples, as well as mathematical derivations, are presented to help the reader understand the sources of these different types artifacts and the way to attenuate them. We also discussed artifacts from the non-interferometric methods and directional noise sources, which directly affect the true dispersion energy and produce biased dispersion information. Finally, we present a brief conclusion, as well as some recommendations, for surface wave dispersion imaging.

In this paper, we use terminology "high-frequency surface wave" to limit the scope of this work to near surface scale including passive-source surface wave surveys with frequency band above 1Hz as well as active-source surface wave surveys with frequency band above 10Hz. The frequency band (> 1Hz) is relatively higher compared to the long period (> 30s) for teleseismic surface waves used in global scale ambient noise applications. We focus on high-frequency (> 1Hz) surface waves because they contribute significantly to urban seismic noise in a broad frequency range from 1Hz to more than 45 Hz with maximum amplitudes between 1 and 10 Hz (Groos and Ritter, 2009). Besides, it is worth noting that this work focuses on the linear receiver array, which is often deployed for both passive-source and active-source surface wave investigations because of its high efficiency and convenience. In populated urban areas, it is challenging to construct dense 2-D arrays due to the spatial restrictions imposed by existing infrastructures. Linear receiver arrays are a natural geometry for road-side investigations utilizing receivers deployed on shoulders or median strip areas. Linear array techniques are also useful when processing distributed acoustic sensing (DAS) data, a recently developed technique which utilizes subsurface fiber-optic cables to capture earth vibrations for seismic imaging (Dou et al., 2017; Ajo-Franklin et al., 2019; Zhan, 2019; Cheng et al., 2021a).

2 Surface wave methods

Figure 1 provides a general data processing flowchart for both the active-source surface wave methods and the passive-source surface wave methods. To explore the underlying physics of the aliasing as well as artifacts, we briefly reviewed the workflow for both the active-source surface wave methods (e.g., MASW) and the passive-source surface wave methods (e.g., MAPS), and introduced the mathematical backgrounds for the corresponding dispersion measurement techniques.

2.1 Active-source surface wave methods

MASW utilizes a multichannel recording system to estimate near-surface S-wave velocity from high-frequency Rayleigh waves. It usually consists of four steps: (a) acquisition of wide-band, high-frequency ground roll using a multichannel recording system (e.g., Song et al., 1989); (2) creation of linear algorithms to transform the time-offset $(x-t)$ domain wavefield into frequency-velocity $(f-v)$ or frequency-wavenumber $(f-k)$ domain dispersion spectra (e.g., Yilmaz, 1987; McMechan and Yedlin, 1981; Park et al., 1998; Xia et al., 2007; Luo et al., 2008); (3) extraction of accurate 1D dispersion curves manually or automatically (e.g., Dai et al., 2020; Ren et al., 2020); (4) development of stable and efficient inversion algorithms to obtain S-wave velocity profiles (e.g., Xia et al., 1999; Wathelet et al., 2004; Maraschini et al., 2010).

Dispersion measurement (imaging) is the vital step for surface wave analysis. Slant-stacking algorithm has been primarily used as an array-based data processing approach to extract phase velocity dispersion information for both land seismic survey (e.g., Xia et al., 2009) and marine seismic survey (e.g., Bohlen et al., 2004). The phase-shift method (Park et al., 1998) is a typical presentation of frequency-domain slant-stacking method, which is popular in the engineering community due to its efficiency and accuracy. Here we take this method for representing to introduce the mathematical background of dispersion imaging, and explore the underlying physics of the sources of the aliasing or artifacts.

Considering the offset-time $(x - t)$ domain representation $u(x, t)$ of a shot gather, the Fourier transform can be applied to the time axis to obtain the frequency-offset $(f - x)$ domain wavefield $U(f, x)$,

$$U(f,x) = \int u(x,t)e^{i2\pi ft}dt, \tag{1}$$

where, the i denotes the imaginary unit. To obtain the frequency-velocity $(f - v)$ domain dispersion spectra, the slant-stacking algorithm is applied on the phase term of $U(f, x)$ (also called the whitened $f - x$ domain wavefield),

$$E(f,v)=\left|\sum_{j=1}^{N} e^{i2\pi f x_j/v}\frac{U(f,x_j)}{|U(f,x_j)|}\right|, \tag{2}$$

where, $E(f,v)$ is the measured dispersion spectra; x_j denotes the offset, $j \in (1..N)$. $e^{i2\pi f x_j/v}$ denotes the phase-shift term associated with the scanning velocity v at frequency f.

Following Aki and Richards (2002), a typical harmonic plane wave $U(f,x)$ can be expressed as

$$U(f,x)=A(f,x)e^{i(\phi_0-2\pi k_0 x)}, \tag{3}$$

where, ϕ_0 is the initial phase term; k_0 is wavenumber which is associated with the theoretical dispersion curve by $k=f/v$. Thus, we can simplify eq.2 by replacing $U(f,x)$ with eq.3,

$$\begin{aligned} E(f,k) &= \left|\sum_{j=1}^{N} e^{i2\pi k x_j}\frac{A(f,x_j)e^{i(\phi_0-2\pi k_0 x_j)}}{|A(f,x_j)e^{i(\phi_0-2\pi k_0 x_j)}|}\right| \\ &= |\sum_{j=1}^{N} e^{i\phi_0}e^{i(2\pi k-2\pi k_0)x_j}| \\ &\approxeq |\sum_{j=1}^{N} e^{i2\pi(k-k_0)x_j}|. \end{aligned} \tag{4}$$

Peaks on $E(f,k)$ will occur where exponent goes to zeros, thus when the scanning wavenumber (k) approaches the true wavenumber (k_0) of the coherent signal.

2.2 Passive-source surface wave methods

Figure 1 also presents the basic data processing schemes for two types of passive-source surface wave methods: the non-interferometric methods (e.g., ReMi (Louie, 2001) and PMASW (Park et al., 2004)), and the interferometric methods (e.g., MAPS (Cheng et al., 2016) and SPAC (Chávez-García et al., 2006)). The key difference between the active-source and passive-source surface wave methods is that the later requires sufficient temporal and/or spectral ensemble averaging/stacking to enhance the coherent signals as well as cancel the incoherent signals from the inhomogeneous noise source distribution.

The data processing workflow before dispersion picking and inversion is made up of four steps:

(1) Observation of the continuous and long-duration ambient noise records. In general, several tens of minutes duration is sufficient for urban passive-source surface wave survey (Cheng et al., 2018b).

(2) Splitting the continuous time series into short overlapped time segments. According to our experiences, a 10s window with a 75% overlap is a good tradeoff between efficiency and signal quality (Cheng et al., 2018b).

(3) Preprocessing on the short time segments to remove potential near-field interferences and extend frequency bandwidth. The basic data preprocessing includes tapering two ends, removing the mean, linear trend, dead traces, as well as instrument response as necessary, temporal normalization, and spectral whitening, for each individual time segment (Bensen et al., 2007; Cheng et al., 2018b).
(4) Dispersion spectra measurement. It is different for the non-interferometric and interferometric methods as indicated in Figure 1 (Cheng et al., 2020). As for the non-interferometric methods (e.g., PMASW and ReMi), active-source surface wave dispersion imaging algorithm will be directly applied on a series of preprocessed narrow time windows and a set of individual dispersion spectra are stacked to obtain the final dispersion spectra. As for the interferometric methods (e.g., MAPS and SPAC), cross-correlation or cross-coherence interferograms between each interstation pair will be calculated and stacked in time before calculating a single final dispersion spectra.

Since the non-interferometric methods employ the same active-source dispersion imaging scheme as we previously described, we will not go through the derivation here. For simplicity, we focus on the interferometric method, MAPS, to introduce the mathematical background of the dispersion imaging.

We follow the conventions in Cheng et al. (2020) to present the cross-correlation spectrum C_{x_1,x_2} as

$$\begin{aligned} C_{x_1,x_2} &= u(x_1,\omega)u^*(x_2,\omega) \\ &= \sum_{j=1}^{N_s}(e^{-i2\pi k_0 x_1}e^{i2\pi k_0 x_2}) + \overline{C_{x_1,x_2}}, \end{aligned} \tag{5}$$

where, $\overline{C_{x_1,x_2}}$ is the cross term; ω is the angle frequency; $u(x_1,\omega)$ and $u(x_2,\omega)$ indicate the ambient noise spectral wavefield following the representation $u(x,\omega) = \sum_{j=1}^{N_s} e^{i(\omega t_{s_i} - 2\pi k_0 r_{s_i} - 2\pi k_0 x)}$ (eq.14 in Cheng et al. (2020)) for the in-line source distribution case.

Because noise sources are assumed to be uncorrelated in time and space, and the contribution of each source to the cross-correlation function could be determined independently (Tromp et al., 2010; Lawrence et al., 2013), the cross term $\overline{C_{x_1,x_2}}$ is negligible given a sufficiently time-averaged ensemble. Applying the ensemble averaging along the time direction yields the cross-correlation spectrum $\langle C_{x_1,x_2}\rangle$ under the in-line source distribution

$$\begin{aligned} \langle C_{x_1,x_2}\rangle &= \langle\sum_{j=1}^{N_s}(e^{-i2\pi k_0 x_1}e^{i2\pi k_0 x_2}) + \overline{C_{x_1,x_2}}\rangle \\ &\approxeq e^{-i2\pi k_0 x_{1,2}}, \end{aligned} \tag{6}$$

where, $\langle ...\rangle$ indicates the ensemble averaging. We employ the slant-stacking algorithm by replacing the wavefield $U(f,x)$ in eq.2 with ensemble averaged cross-correlation spectrum $\langle C_{x_1,x_2}\rangle$ to obtain the MAPS representation

$$E(f,k) = |\sum_{m=1}^{N-1}\sum_{n=m+1}^{N} e^{i2\pi k x_{m,n}} \frac{\langle C_{x_m,x_n}\rangle}{|\langle C_{x_m,x_n}\rangle|}| \\ = |\sum_{m=1}^{N-1}\sum_{n=m+1}^{N} e^{i2\pi(k-k_0)x_{m,n}}|, \tag{7}$$

where, $\sum_{m=1}^{N-1}\sum_{n=m+1}^{N}$ denotes the C_N^2 inter-station cross-correlation pairs. The energy peaks of $E(f,k)$ will occur where the scanning wavenumber (k) approaches the true wavenumber (k_0) of the coherent signal. Eq.7 demonstrates the ability of the interferometric method to produce the accurate dispersion curve. It is almost identical to eq.4 but with more and denser receiver pairs. It explains the similarity of dispersion measurements between active-source surface wave methods and interferometric surface wave methods once we are confident on the retrieved signals from virtual sources (e.g., Green's function or spatially averaged coherency). The reader is referred to Cheng et al. (2020) for more details about the derivation for passive-source surface wave dispersion imaging, including the approximation and bias of the non-interferometric method.

3 Artifacts in surface wave dispersion imaging

Although the active-source surface wave surveys usually provide much better and cleaner dispersion spectra than the passive-source surveys, aliasing or artifacts are still inevitable. We summarize three types of artifacts that are frequently observed on surface wave dispersion spectra, and explore the underlying physics of the sources of these artifacts, as well as the solutions to attenuate them.

Note that as review work, all field examples included in this work have already been reported before for various purposes and most of the details about data collection and basic data processing have been omitted to make room for the discussion on artifacts. The reader is invited to the corresponding references for more details. For clearer presentation, all dispersion images in this work, except in Figure 10, have been normalized along the frequency direction.

3.1 Artifacts from sparse spatial sampling

Spatial aliasing is an artifact due to undersampling or poor reconstruction, and is usually related to the high frequencies. Several studies have been carried out to understand the aliasing (Turner, 1990; Li et al., 1991; Rafaely et al., 2007; Yan et al., 2016; Dai et al., 2018). In this work, we present a unique perspective on the source of spatial aliasing in surface wave dispersion imaging.

Based on the derivations for the surface wave dispersion measurement (eq.4 and eq.7), the energy peaks of $E(f,k)$ will occur when the scanning wavenumber $k = f/v$ approaches the true dispersion curve k_0 of the coherent signal. Due to the similarity between eq.4 (active-source) and eq.7 (passive-source), we focus on the later to explore the underlying physics of spatial aliasing. Besides, the spatial aliasing is usually not a serious issue for the active-source surface wave surveys due to the dense sampling acquisitions.

Given the evenly sampled acquisition system, which is commonly used in shallow-structure surface wave survey, we define $x_{m,n} = (m-n) * dx$ for simplicity, where dx denotes the spatial interval. We modify eq.7 using Euler formula as

$$\begin{aligned} E(f,k) &= |\sum_{m=1}^{N-1}\sum_{n=m+1}^{N} e^{i2\pi(k-k_0)x_{m,n}}| \\ &= |\sum_{m=1}^{N-1}\sum_{n=m+1}^{N} cos\{2\pi(k-k_0)x_{m,n}\} + i * sin\{2\pi(k-k_0)x_{m,n}\}| \\ &= |\sum_{m=1}^{N-1}\sum_{n=m+1}^{N} cos\{2\pi(m-n)(k-k_0)dx\} + i * sin\{2\pi(m-n)(k-k_0)dx\}|. \end{aligned} \tag{8}$$

According to the periodicity of a trigonometric function, k_0 is not the unique solution of eq.8. We list four aliasing solutions as follows:

$$k = k_0 - \frac{j}{dx},\ (k_0 > 0) \tag{9a}$$

$$k = k_0 + \frac{j}{dx},\ (k_0 > 0) \tag{9b}$$

$$k = -k_0 + \frac{j}{dx},\ (k_0 < 0) \tag{9c}$$

$$k = \frac{j}{dx},\ (k_0 \ll dx) \tag{9d}$$

where, j denotes an non-negative integer. Given a sufficient large dx, the aliasing k in eq.9 would possess a high possibility to be visible at the target window around k_0. It presents the underlying physics of four types of aliasing energy that could be observed on surface wave dispersion spectra, particularly for the sparse geometry cases. Figure 2 clearly illustrates the characteristics of four types of spatial aliasing in terms of different spatial intervals, $dx = 2m$ (Fig.2a) and $dx = 10m$ (Fig.2b). We introduce three field examples to help the reader understand these different types of spatial aliasing.

3.1.1 Spatial aliasing artifacts: type A and type B

According to eq.9a and 9b, the type A spatial aliasing is less likely to be visible on the low velocity surface wave target window compared to type B, because of the smaller wavenumber value which indicates the higher velocity value for a specific frequency. It is seldom to observe both types of spatial aliasing on the same surface wave dispersion image (Foti et al., 2018). However, cautions should be used towards the type A spatial aliasing since it might be recognized as the higher modes of the surface waves and cause mode misidentification (Dai et al., 2018).

To introduce these two types of artifacts, we present a typical example which was first reported by Hu et al. (2016). Figure 3a shows a 145-channel common-shot-point (CSP) gather with 10m spatial interval and 29.5m nearest offset, and both surface waves (ground-roll wave) and body waves are visible. Figure 3b displays the dispersion spectra obtained by using the phase-shift method. The multi-mode surface waves energy with low velocity (< 0.5km/s) and low frequency (< 10Hz) characteristics can be observed at the bottom left, and the dispersion spectra are dominated by the non-dispersive body waves, which are represented by the strong horizontal dispersion energy belts around 1.8km/s (the blue dotted line). Weak air wave energy is also visible at a velocity around 0.34km/s as indicated by the red dotted line. Based on eq.9, we are able to predict any type of spatial aliasing for all observed wave types by replacing the objective dispersion curve $k_0(w)$ with the picks of surface waves, body waves, and air waves. We eventually found the type A spatial aliasing from air wave and the type B spatial aliasing from the body wave are located inside the spectra window, and match well with the artifacts energy at the top right (the red diamond curves) and the bottom right (the blue dash-dot curves), respectively. The good match between the predicted aliasing and the observed artifacts convinces us of the derivation of spatial aliasing (eq.9). Note that, we did not present the predicted aliasing of surface waves since it is beyond the current spectra window with velocities lower than 0.1km/s at a frequency band 1∼9Hz.

3.1.2 Spatial aliasing artifacts: type C

According to eq.9c, the type C spatial aliasing will occur when $k_0 < 0$. It indicates the slant-stacking algorithm is scanning a reverse (backward) propagating surface wave train instead of the expected forward propagating one ($k_0 > 0$). Also, eq.9c is consistent with the finding of Cheng et al. (2018b), which first demonstrated the existence of a type of "crossed" aliasing due to the bidirectional velocity scanning scheme in passive-source surface wave dispersion analysis. It usually occurs on the dispersion measurements of the non-interferometric passive-source surface wave methods, which technically sum the dispersion spectra from both the forward and the reverse directions to account for the possible bidirectional nature of the recorded ambient surface waves (Park et al., 2004; Cheng et al., 2018b). In general, the summation operator in the non-interferometric methods is a reasonable trade-off because of the unknown propagation direction of the incoming surface waves. However, this ambiguity can produce the “crossed” aliasing in dispersion measurement, which is exactly the type C spatial aliasing discussed in this work, and the “crossed” aliasing could seriously smear the dispersion energy, particularly at the higher frequency band and the higher order components.

We present an example of the type C spatial aliasing in Figure 4 from 10-min traffic noise records with a 24 vertical-component receiver array. The spatial interval is 10m. The dataset was first reported by Cheng et al. (2018b). We observe the "crossed" aliasing on dispersion spectra of the non-interferometric methods, PMASW (Fig.4a) and ReMi (Fig.4b), due to the bidirectional slant-stacking scheme; while MAPS method produces a clean dispersion image (Fig.4d) because the direction of the scanning velocity has been defined as from virtual sources to virtual receivers. To attenuate this type of aliasing, Cheng et al. (2018b) provided an effective technique with FK-based data-selection, and Xi et al. (2020) proposed to use the SVD (singular value decomposition) based Wiener filter. Note that, the existence of weak "crossed" aliasing on the SPAC measurement (Fig.4c) is a special case since the bidirectional slant-stacking scheme does not apply here. Instead, it is supposed to be associated with the systematic bias of SPAC due to directional aliasing (Cho et al., 2008). Considering the periodicity and symmetry characteristic of Bessel function or Hankel function (Forbriger, 2003; Cho et al., 2008), and it is likely to attenuate these directional aliasing by replacing the Bessel function used in SPAC fitting with the adaptive Hankel functions (Xi et al., 2021).

Based on eq.9c, we predict the spatial aliasing by using the picked multi-mode dispersion curves from MAPS measurement (the black dots on Fig.4). The predicated type C spatial aliasing generally fits the "crossed" artifacts (the cyan dots on Figs.4a, b and c), although distortions exist due to the picking biases. Besides, the predicted type B spatial aliasing (the blue dots on Figs.4a, b, c, and d) also matches the linear artifacts at the bottom right of the spectra window. Note that, the little off between the picked dispersion curves from MAPS and the energy peaks of the non-interferometric methods (Figs.4a and b) reflects the biases of the non-interferometric methods (Cheng et al., 2020) which will be discussed later.

3.1.3 Spatial aliasing artifacts: type D

According to eq.9d, the type D spatial aliasing is independent of the true dispersion energy, and presents as a series of linear strips on the $f-v$ domain (or a series of paralleled horizontal lines on the $f-k$ domain). Figure 5 shows an example of the type D spatial aliasing. The dataset consists of 16 days ambient noise data recorded by 35 broadband seismometers (Trillium 120 P/PA), which has been reported by Xu et al. (2016) and Pan et al. (2016b). The spatial interval is around 1km. We apply ambient noise interferometry (cross-coherence) to retrieve the coherent Rayleigh waves from the vertical component. We stack over all the inter-station pairs of empirical Green's functions into discrete 1km offset bins (Fig.5a) to further enhance the retrieved coherent signals. Figure 5b displays the obtained dispersion spectra using MAPS. The distinct linear artifacts that cross the fundamental dispersion energy can be distinguished as the type D spatial aliasing using the predicted aliasing (the green dashed line) based on eq.9d.

Since the type D spatial aliasing presents as linear artifacts with constant wavenumber, it can be easily attenuated in $f-k$ domain using filter techniques, for example, the median filter (Duncan and Beresford, 1995) and the FK filter (Zhou, 2014). Figure 5c displays an example of aliasing attenuation using the FK filter. The dispersion spectra have been improved with the extended frequency bandwidth and the attenuated distortions at low frequencies. However, some weak linear aliasing artifacts still exist at high frequency due to the leakage of the FK filter.

According to the Nyquist theorem, we can define the maximum wavenumber as the two times of the Nyquist wavenumber, $k_{max} = 2 * \frac{1}{2*dx} = \frac{1}{dx}$. k_{max} can be taken as an effective quality control factor for surface wave dispersion imaging, and provide a reasonable reference for the maximum frequency boundary.

3.2 Array response artifacts

Array geometry configuration is vital for seismic acquisitions. Here we employ the array response function (ARF) concept to present the influence of the array geometry on dispersion measurement (Capon, 1969b; Rost and Thomas, 2002; Picozzi et al., 2010; Liu et al., 2020). The array response function is also called the array smoothing function (ASF) or the spectral estimator in some literatures (Johnson and Dudgeon, 1993; Boiero and Socco, 2011; Bergamo et al., 2012). We define the ARF as

$$ARF(k) = |\sum_{j=1}^{N} e^{i(k-k_0)x_j}|. \tag{10}$$

For comparison, two numerical tests with different array lengths, 50m (Fig.6a) and 250m (Fig.6b), are carried out to generate 15-min ambient noise records with random distributed sources configurations. The reader is referred to Cheng et al. (2016) for more details about ambient noise modeling. Figure 7a presents the corresponding normalized ARFs for two arrays. We observe the ARF curve (the pink curve) of the shorter array posses the broader main lobe (lower kurtosis) and distinct side lobes. As for the slantstacking-based dispersion imaging methods, the main lobe of the ARF determines the imaging resolution (Boiero and Socco, 2011; Cheng et al., 2020). Figure 7b and Figure 7c present the obtained dispersion spectra using the MAPS method from two arrays, respectively. We overlay the dispersion spectra with the corresponding ARF curve. For a specific frequency, i.e. 17Hz, the main lobes of the ARFs match well with the dominant dispersion energy bandwidth, and the peaks of ARFs are consistent with the peaks of the accurate dispersion energy. In general, the shorter array produces the lower resolution spectral image, and vice versa.

The weak wiggles around the dominant dispersion energy (as indicated by the black arrows on Fig.7b) coincide with the side lobes of the ARFs, and are taken as artifacts from the array response. In practice, the array response artifacts on dispersion spectra might be misidentified as weak higher modes. Moreover, the artifacts (wiggles) could emphasize smearing from the incoherent noise on the dispersion spectra. Cheng et al. (2021b) proposed a phase-weighted slant-stacking technique for surface wave dispersion measurement to attenuate array response artifacts on dispersion spectra.

Eq.9 demonstrates the spatial aliasing is directly associated with the spatial sampling interval (dx), which controls the maximum wavenumber sampled using the array. Whereas, the length of the array (L) determines the minimum resolvable wavenumber ($k_{min} = 1/L$). k_{min} can be taken as the absolute wavenumber resolution (or the imaging resolution of the surface wave dispersion spectra) according to the Fourier analysis. Besides, k_{min} also controls the bottom frequency boundary of the dispersion measurement since the minimum wavenumber is linearly associated with the lowest frequency. We carry out two similar numerical tests based on two linear arrays with different array lengths, 100m and 20m, to generate 15-min ambient noise records with the same random distributed source configuration as indicated in Figure 6. We apply the MAPS method to the generated noise records from two arrays for dispersion imaging. Note that no data preprocessing operator is included prior to noise cross-correlation to avoid potential effects from the pre-processing operators, like spectra whitening, on the frequency bandwidth of the measured dispersion spectra. Figure 8 shows that the true dispersion curve fits the obtained dispersion spectra when the scanning wavenumber k is greater than the minimum resolvable wavenumber k_{min} (the pink dashed line). The dispersion energy turns to be biased when $k > k_{min}$, because the scanning wavenumber is beyond the absolution resolution of wavenumber.

To avoid artifacts due to array aperture, therefore, we can employ k_{min} as an approximate quality control indicator. It is worth noticing that k_{min} is not a strict limitation, because in practice the retrieved minimum scanning wavenumber is possible to go beyond k_{min}, particularly for the passive-source surface wave surveys, which might be relevant to the specific data processing algorithms.

3.3 Artifacts from weak coherent signals: the radial pattern artifacts

The observed frequency band of seismic records is finite, and usually depends on the source spectrum distribution. In general, the dominant frequency band is usually located above 10Hz for the sledgehammer activated surface waves, and from 1Hz to 10Hz for the traffic-induced surface waves in an urban area. If we force the mathematical algorithms to measure surface wave dispersion spectra beyond the recorded frequency band, artifacts will be introduced. For example, given $U(f, x)$ is a tiny value, the computation of $U(f, x)/|U(f, x)|$ in eq.2 will be unstable. For the scanning frequencies beyond the acceptable frequency band, the measurement of eq.4 will be dominated by the term $e^{i2\pi kx}$, which is associated with the array response and frequency-independent. Thus, it will produce artifacts with constant wavenumber values which present as radial pattern energy on $f - v$ domain dispersion spectra. We call these types of artifacts, radial pattern artifacts. Note that, the type D spatial aliasing is one special case of radial pattern artifacts.

Here, we present one active-source numerical example and two passive-source field examples to introduce the radial pattern artifacts, and more importantly discuss the influences from different data processing procedures on attenuation of this type of artifacts.

3.3.1 Numerical example

An active-source surface wave shot gather from a two-layer earth model (Table.2) was generated using a finite-difference solver, SOFI2D (Bohlen, 2002), with a 25Hz ricker wavelet and 30m nearest offset. Figure 9a shows the synthetic Rayleigh wave observed with a 60-channel linear receiver array with 1m spatial interval. Figure 9b displays the corresponding dispersion measurement obtained using the phase-shift method. We can observe distinct radial pattern energy at the high frequency (> 65Hz) band as well as noisy artifacts at the lower frequency (< 5Hz) band. After spectral analysis, we find these artifacts at the two ends (below 5Hz and above 65Hz, indicated by the blue dashed lines) are co-located with the weak spectrum energy, where the spectrum amplitudes are approaching zero (Fig.9c).

To better display the characteristic of the radial pattern artifacts, we present the obtained dispersion spectra without frequency-direction normalization on both $f - k$ domain (the top panels on Fig.10) and $f - v$ domain (the bottom panels on Fig.10), respectively. A series of horizontal artifacts (indicated by the black arrows) are shown at two ends on the $f - k$ domain dispersion spectra, which are co-located with the radial pattern artifacts on the $f - v$ domain dispersion spectra. It coincides with our previous discussions that dispersion imaging beyond the recorded frequency band will produce radial pattern artifacts. Besides, we can also distinguish the consistent wiggles (artifacts) from 2Hz to 9Hz (highlighted by the pick box on Fig.10a), which consist of two parts: the radial pattern artifacts at lower frequency (< 5Hz) and the array response artifacts at the higher frequency (> 5Hz). It implies the similarity between the radial pattern artifacts and the array response, and also the possibility to attenuate the radial pattern artifacts by techniques designed for attenuation of the array response artifacts as previously described.

3.3.2 Field example #1

Figure 11 presents a passive-source field example of the radial pattern artifacts. 5-min ambient noise data were recorded by a linear array of 38 Zland nodes (5 Hz) with 2ms sampling rate and 1m spatial-interval. The dataset was first reported by Liu et al. (2020). Figure 11a shows the bin-stacked virtual source gather retrieved from ambient noise interferometry without noise data whitening preprocessing (Bensen et al., 2007). We apply the MAPS method for dispersion analysis. The obtained dispersion spectra present two distinct radial pattern artifacts as highlighted by the black dashed line. We can also observe weak spatial aliasing at the bottom right.

After including the whitening preprocessing procedure prior to the cross-correlation, whereas, we observe the mentioned two types of artifacts have been significantly eliminated (Fig.12a). Spectral whitening is an important data preprocessing technique, which aims to balance the noise spectrum and extend the frequency bandwidth of the retrieved coherent signals from ambient noise interferometry. In order to display the influences of the spectral whitening, we apply spectral analysis on the extracted cross-correlations with (the pink curve on Fig.12b) and without (the dark blue curve on Fig.12b) whitening. After whitening, the spectrum had been significantly extended at lower frequency band (< 5Hz), and balanced at higher frequency band (> 15Hz). It indicates spectral whitening makes a contribution to attenuation of the radial pattern artifacts for passive-source surface wave dispersion imaging.

According to Prieto et al. (2009), performing cross-correlation C_{x_1,x_2} with spectral whitening is equivalent to calculating the cross-coherence H_{x_1,x_2},

$$H_{x_1,x_2} = \frac{u(x_1,\omega)u^*(x_2,\omega)}{|u(x_1,\omega)||u(x_2,\omega)|}. \tag{11}$$

In terms of attenuation of the radial pattern artifacts, our work indicates the advantage of cross-coherence over cross-correlation in passive-source surface wave imaging (Nakata et al., 2011). Caution should be used because pseudo arrivals generated by spectral whitening or cross-coherence with scattered waves can occur, particularly for at low frequencies (Nakata, 2020). Besides, it is interesting that some spikes on the spectrum (e.g., 22Hz, 31Hz, 39Hz on the pink curves) seem to be enhanced after whitening, which are also co-located with the spikes (or gaps) on the dispersion spectra and might be associated with some persistent noise sources around the site. To remove these spikes on dispersion spectra, the conventional spectral de-spiking processing (Girard and Shragge, 2019) does not seem to apply here, and further studies are required.

3.3.3 Field example #2

According to eq.7, MAPS includes the whole C_N^2 inter-station cross-correlation pairs for dispersion imaging. For many interferometric passive-source surface wave applications, however, only one shot gather (C_N^1) with virtual-source located at one end of the receiver array is utilized (e.g., Zhang et al., 2020; Li et al., 2020), because the interpreter still follows the conventional active-source surface wave (e.g., MASW) acquisition strategy by using single shot gather for dispersion analysis. In this case, much useful information will be wasted, and the measurement from one virtual-source gather might be different with that from multiple virtual-sources gather since the array responses of these two geometry configurations are different. Here we take an array of 24 sensors with 10m spatial interval as example, and estimate ARF for both one virtual-source gather (C_N^1 inter-station pairs) and multiple virtual-sources gather (C_N^2 inter-station pairs). Compared with the former (the red dashed curve on Fig.13), the later (the black curve on Fig.13) shows smoother side lobes which might decrease the possibility of the interference between the array response artifacts and the incoherent noise.

We present an example to show the performances of the interferometric method (i.e. MAPS) with different virtual-source gathers. The dataset was first reported by Cheng et al. (2019), which was collected along a busy railway over 30-min using a 24-channel linear array. The spatial interval is 10m. Ambient noise interferometry is applied to retrieve empirical Green's functions. Figure 14a presents the configuration of virtual source and virtual receiver for the multiple virtual-sources gather. Figure 14b displays the retrieved C_N^2 inter-station cross-correlation pairs. MAPS is then performed with only one virtual-source gather (highlighted by the yellow box) and with the whole multiple virtual-sources gather. Compared with the dispersion measurement from one virtual-source gather (Fig.15a), the dispersion measurement from multiple virtual-sources gather (Fig.15b) is more continuous and much cleaner with fewer distortions and radial pattern artifacts.

Although spectral whitening has been included during data preprocessing, radial pattern artifacts somehow still exist (indicated by the black dashed lines in Figure 15), which indicates spectral whitening is not universally applicable for radial pattern artifacts attenuation. Data-selection is an effective tool for data quality control, and might be an alternative. We refer to Cheng et al. (2019) to present a successful application of radial pattern artifacts attenuation by automatic data-selection in $\tau - p$ domain. Figure 16 shows that the dispersion spectra have been much improved with the radial pattern artifacts significantly attenuated. The reader is referred to Cheng et al. (2019) for more details about the data-selection technique. Studies have successfully applied data-selection on passive-source surface wave imaging for dispersion spectra enhancement (e.g., Cheng et al., 2018b; Zhou et al., 2018; Cheng et al., 2019; Pang et al., 2019).

4 Discussion

As the first review work on the artifacts in surface wave dispersion imaging, we admit that we might not be able to include all the existing artifacts but the summarized three types of artifacts in this work are significant to understanding the complexity of surface wave dispersion imaging and lay a foundation for the further work.

All previously mentioned artifacts, including spatial aliasing, array response artifacts, and radial pattern artifacts, present as individual energy overlying around the true dispersion energy and smearing peaks of the true dispersion energy. Meanwhile, there also exist some artifacts that directly affect the true dispersion energy and produce biased dispersion information. Here, we discuss two types of these artifacts: artifacts from the non-interferometric passive-source methods, and artifacts from the directional noise sources.

4.1 Artifacts from the non-interferometric passive-source methods

Cheng et al. (2020) presents a comprehensive comparison between the non-interferometric methods and the interferometric methods. Numerical tests and field examples demonstrate that the non-interferometric methods are less accurate than the interferometric methods when sources are out of line. Compared with the accurate dispersion spectra obtained from the interferometric methods, these biased dispersion energy measured by the non-interferometric methods can be taken as artifacts.

Here we present an example of the artifacts from the non-interferometric methods. The dataset was first reported by Cheng et al. (2020). A linear array of 48 RefTek 125A digitizers was deployed parallel to a busy road with an off-line distance 20∼30m. All digitizers were connected to 2.5 Hz vertical-component geophones. Figure 17 presents a comparison of the obtained dispersion spectra between the non-interferometric methods, PMASW (Fig.17a) and ReMi(Fig.17b), and the interferometric methods, SPAC (Fig.17c) and MAPS (Fig.17d). The little off between the picked dispersion curves from MAPS (the black crosses) and the energy peaks of the non-interferometric methods indicates the biases produced by the non-interferometric methods. To address the biases, Louie (2001) indicated that an interpreter must pick the lower edge of energy peaks of phase velocities on the ReMi measurements, rather than the dispersion energy peaks, and hypothesized that the off-line triggered sources caused the higher apparent velocities. However, this bias phenomenon is not unique to the ReMi method but is common to all linear-array-based non-interferometric passive-source surface wave methods. Cheng et al. (2020) provided a way to estimate the biases in non-interferometric measurements by using the defined array smoothing function (ASF).

4.2 Artifacts from directional noise sources

It is well known that the empirical Green's function can be extracted by cross-correlating two receivers under the randomly distributed noise sources. In practice, the noise source distribution is never perfectly random. Cheng et al. (2016) presented that the directional noise sources could produce biased cross-correlations, as well as biased dispersion measurements, particularly for linear receiver arrays. In order to attenuate the azimuthal effect on dispersion measurements, Cheng et al. (2016) proposed to apply azimuthal adjustment to the slant-stacking algorithm. However, it remains a real challenge for azimuth detection using linear array. To address the problem with the frequently-used linear array, Liu et al. (2020) adapted a linear receiver array into a pseudo-linear array by adding two more off-line receivers to increase the array response to off-line signals.

We apply the 2D ARF concept to explain the limitation of the linear array. For consistency, we simply adapt the ARF on eq.10 from 1D to 2D as,

$$ARF(k,\theta) = |\sum_{j=1}^{N} e^{ik(x_j cos\theta + y_j sin\theta) - ik_0(x_j cos\theta_0 + y_j sin\theta_0)}|, \tag{12}$$

where, x_i and y_i indicate the receiver location in Cartesian coordinates. Since 2D ARF can illustrate the array response or beamforming resolution to a plane wave, we take a plane wave at frequency 15Hz and velocity 0.3km/s as example. Figure 18 presents a comparison of ARFs between the linear array (the left panel) and the pseudo-linear array (the right panel). The linear array provides multiple beamer peaks which can not focus on the target azimuth and velocity (the pink circle); while the adapted pseudo-linear array shows a high resolution response to the input plane wave. It implies the linear array can not solve the 2D beamforming problems that simultaneously seeks azimuth and velocity. Thus, Cheng et al. (2016) suggested defining an average velocity for azimuth detection, while the pseudo-linear array geometry provides a solution cleverly.

5 Conclusions

We summarize three types of artifacts that are frequently observed on surface wave dispersion measurements, including the artifacts from sparse spatial sampling, array response artifacts, and artifacts from weak coherent signals. Numerical and field examples present how these artifacts are generated and how these artifacts can be attenuated. This work might help the reader understand the complexity of the measured dispersion spectra and lead to further improvement on surface wave dispersion analysis. It also suggests:

(1) the shorter spatial interval dx will extend the maximum wavenumber k_{max}, and result in higher maximum frequency limitation that can be observed on dispersion spectra;

(2) the longer array length L will increase the dispersion imaging resolution with the smaller minimum wavenumber k_{min}, and result into lower minimum frequency limitation that can be observed on dispersion spectra;

(3) the spectral whitening is critical to broadening frequency bandwidth for surface wave dispersion imaging, particularly for the passive-source surface wave imaging;

(4) the cross-coherence algorithm is recommended for the applications of the interferometric surface wave methods, since it has the advantage of including spectral whitening when cross-correlating;

(4) the multiple virtual-sources gather (C_N^2) is prior to the one virtual-source gather (C_N^1) for the interferometric surface wave imaging, which will increase the data utilization and enhance the coherent dispersion energy.

Considering the limitation of the expense budget for the expensive instruments, the shorter spatial interval and the longer array length are always in conflict for the conventional nodal-based or cable-based seismic survey. We have to make a trade-off between the higher frequency limitation with the denser array and the lower frequency requirement with the longer array. However, recent advances in distributed acoustic sensing (DAS) acquisition provide routes to solve these problems; DAS in particular allows for acquisition over tens of kilometers while providing spatial sampling in the meter range, thus enabling local surface wave analysis with high fidelity.

Acknowledgements This study was supported by the National Natural Science Foundation of China under grant no. 41830103. We thank the SISL team, as well as AoCheng Tech crews, for the field-data acquisitions. We would like to thank Changjiang Zhou, Chaoqiang Xi, Jingyin Pang, Tianyu Dai and Ya Liu for many useful discussions. Finally, we thank the Editor and two anonymous reviewers for their constructive and detailed comments that significantly improved our paper.

Conflict of interest

The authors declare that they have no conflict of interest.

References

Ajo-Franklin JB, Dou S, Lindsey NJ, Monga I, Tracy C, Robertson M, Rodriguez Tribaldos V, Ulrich C, Freifeld B, Daley T, Li X (2019) Distributed Acoustic Sensing Using Dark Fiber for Near-Surface Characterization and Broadband Seismic Event Detection. Scientific Reports 9(1):1328, DOI 10.1038/s41598-018-36675-8

Aki K (1957) Space and time spectra of stationary stochastic waves, with special reference to microtremors. Bulletin of the Earthquake Research Institute 35:415–456

Aki K (1965) A Note On The Use Of Microseisms In Determining The Shallow Structures Of The Earth's Crust. GEOPHYSICS 30(4):665–666, DOI 10.1190/1.1439640

Aki K, Richards PG (2002) Quantitative seismology. University Science Books

Ali MY, Barkat B, Berteussen KA, Small J (2013) A low-frequency passive seismic array experiment over an onshore oil field in Abu Dhabi , United Arab Emirates. Geophysics 78(4):B159–B176

Asten MW (2006) On bias and noise in passive seismic data from finite circular array data processed using SPAC methods. Geophysics 7(6):153–162

Bakulin A, Calvert R (2006) The virtual source method: Theory and case study. Geophysics 71(4):139–150

Behm M, Leahy GM, Snieder R (2014) Retrieval of local surface wave velocities from traffic noise - an example from the La Barge basin (Wyoming). Geophysical Prospecting 62(2):223–243

Bensen GD, Ritzwoller MH, Barmin MP, Levshin AL, Lin F, Moschetti MP, Shapiro NM, Yang Y (2007) Processing seismic ambient noise data to obtain reliable broad-band surface wave dispersion measurements. Geophysical Journal International 169:1239–1260

Bergamo P, Boiero D, Socco LV (2012) Retrieving 2D structures from surface-wave data by means of space-varying spatial windowing. Geophysics 77(4):EN39, DOI 10.1190/geo2012-0031.1

Bohlen T (2002) Parallel 3-d viscoelastic finite difference seismic modelling. Computers & Geosciences 28(8):887–899

Bohlen T, Kugler S, Klein G, Theilen F (2004) 1.5D inversion of lateral variation of Scholte-wave dispersion. Geophysics 69(2):330, DOI 10.1190/1.1707052

Boiero D, Socco LV (2011) The meaning of surface wave dispersion curves in weakly laterally varying structures. Near Surface Geophysics 9:561–570, DOI 10.3997/1873-0604.2011042

Campillo M, Paul A (2003) Long-range correlations in the diffuse seismic coda. Science 299(5606):547–549

Capon J (1969a) High-resolution frequency-wavenumber spectrum analysis. Proceedings of the IEEE 57(8):1408–1418

Capon J (1969b) High-Resolution Frequency-Wavenumber Spectrum Analysis. Proceedings of The IEEE 57(8):1408–1418

Castellanos JC, Clayton RW, Juarez A (2020) Using a Time-Based Subarray Method to Extract and Invert Noise-Derived Body Waves at Long Beach, California. Journal of Geophysical Research: Solid Earth 125(5), DOI 10.1029/2019JB018855

Chávez-García FJ, Rodríguez M, Stephenson WR (2006) Subsoil structure using SPAC measurements along a line. Bulletin of the Seismological Society of America 96(2):729–736, DOI 10.1785/0120050141

Cheng F, Xia J, Xu Y, Xu Z, Pan Y (2015) A new passive seismic method based on seismic interferometry and multichannel analysis of surface waves. Journal of Applied Geophysics 117:126–135

Cheng F, Xia J, Luo Y, Xu Z, Wang L, Shen C, Liu R, Pan Y, Mi B, Hu Y (2016) Multi-channel analysis of passive surface waves based on cross-correlations. Geophysics 81(5):EN57–EN66

Cheng F, Xia J, Shen C, Hu Y, Xu Z, Mi B (2018a) Imposing active sources during high-frequency passive surface-wave measurement. Engineering 4(5):685–693

Cheng F, Xia J, Xu Z, Hu Y, Mi B (2018b) Frequency – Wavenumber (FK)-Based Data Selection in High - Frequency Passive Surface Wave Survey. Surveys in Geophysics 39:661–682

Cheng F, Xia J, Behm M, Hu Y, Pang J (2019) Automated Data Selection in the Tau–p Domain: Application to Passive Surface Wave Imaging. Surveys in Geophysics pp 1–18, DOI 10.1007/s10712-019-09530-2

Cheng F, Xia J, Xu Z, Ajo-Franklin J (2020) Comparisons between non-interferometric and interferometric passive surface wave imaging methods - Towards linear receiver array. In: SEG Technical Program Expanded Abstracts 2020, Society of Exploration Geophysicists, pp 2110–2114

Cheng F, Chi B, Lindsey NJ, Dawe TC, Ajo-Franklin JB (2021a) Utilizing distributed acoustic sensing and ocean bottom fiber optic cables for submarine structural characterization. Scientific Reports 11(1):5613, DOI 10.1038/s41598-021-84845-y

Cheng F, Xia J, Zhang K, Zhou C, Ajo-Franklin JB (2021b) Phase-weighted slant-stacking for surface wave dispersion measurement. Geophysical Journal International pp 256–269, DOI 10.1093/gji/ggab101

Cho I, Tada T, Shinozaki Y (2008) Assessing the applicability of the spatial autocorrelation method: A theoretical approach. Journal of Geophysical Research 113(B6):1–19, DOI 10.1029/2007jb005245

Dai T, Hu Y, Ning L, Cheng F, Pang J (2018) Effects due to aliasing on surface-wave extraction and suppression in frequency-velocity domain. Journal of Applied Geophysics 158:71–81, DOI 10.1016/j.jappgeo.2018.07.011

Dai T, Xia J, Ning L, Xi C, Liu Y, Xing H (2020) Deep Learning for Extracting Dispersion Curves. Surveys in Geophysics (August), DOI 10.1007/s10712-020-09615-3

Dorman J, Ewing M (1962) Numerical inversion of seismic surface wave dispersion data and crust-mantle structure in the new york-pennsylvania area. Journal of Geophysical Research 67(13):5227–5241

Dou S, Lindsey N, Wagner AM, Daley TM, Freifeld B, Robertson M, Peterson J, Ulrich C, Martin ER, Ajo-Franklin JB (2017) Distributed Acoustic Sensing for Seismic Monitoring of The Near Surface: A Traffic-Noise Interferometry Case Study. Scientific Reports 7(1):11620, DOI 10.1038/s41598-017-11986-4

Draganov D, Campman X, Thorbecke J, Verdel A, Wapenaar K (2009) Reflection images from ambient seismic noise. Geophysics 74(5):A63–A67

Duncan G, Beresford G (1995) Median filter behaviour with seismic data 1. Geophysical prospecting 43(3):329–345

Eslick R, Tsoflias G, Steeples D (2008) Field investigation of love waves in near-surface seismology. Geophysics 73(3):G1–G6

Forbriger T (2003) Inversion of shallow-seismic wavefields: I. Wavefield transformation. Geophysical Journal International 153(3):719–734, DOI 10.1046/j.1365-246X.2003.01929.x

Foti S, Parolai S, Albarello D, Picozzi M (2011) Application of surface-wave methods for seismic site characterization. Surveys in geophysics 32(6):777–825

Foti S, Hollender F, Garofalo F, Albarello D, Asten M, Bard PY, Comina C, Cornou C, Cox B, Di Giulio G, et al. (2018) Guidelines for the good practice of surface wave analysis: A product of the interpacific project. Bulletin of Earthquake Engineering 16(6):2367–2420

Girard AJ, Shragge J (2019) Automated processing strategies for ambient seismic data. Geophysical Prospecting pp 1–20, DOI 10.1111/1365-2478.12794

Groos JC, Ritter JRR (2009) Time domain classification and quantification of seismic noise in an urban environment. Geophysical Journal International 179(2):1213–1231, DOI 10.1111/j.1365-246X.2009.04343.x

Haney MM, Mikesell TD, van Wijk K, Nakahara H (2012) Extension of the spatial autocorrelation (spac) method to mixed-component correlations of surface waves. Geophysical Journal International 191(1):189–206

Hu Y, Wang L, Cheng F, Luo Y, Shen C, Mi B (2016) Ground-roll noise extraction and suppression using high-resolution linear Radon transform. Journal of Applied Geophysics 128:8–17, DOI 10.1016/j.jappgeo.2016.03.007

Ivanov J, Park CB, Miller RD, Xia J (2005) Analyzing and Filtering Surface-Wave Energy By Muting Shot Gathers. Journal of Environmental & Engineering Geophysics 10(3):307–322

Johnson D, Dudgeon D (1993) Array signal processing: Ptr prentice hall. Englewood Cliffs, N J p 533

Lacoss RT, Kelly EJ, Toksöz MN (1969) Estimation of seismic noise structure using arrays. Geophysics 34(1):21–38

Lawrence JF, Denolle M, Seats KJ, Prieto Ga (2013) A numeric evaluation of attenuation from ambient noise correlation functions. Journal of Geophysical Research: Solid Earth 118(12):6134–6145

Le Feuvre M, Joubert A, Leparoux D, Côte P (2015) Passive multi-channel analysis of surface waves with cross-correlations and beamforming. application to a sea dike. Journal of Applied Geophysics 114:36–51

Lepore S, Grad M (2020) Relation between ocean wave activity and wavefield of the ambient noise recorded in northern poland. Journal of Seismology 24(6):1075–1094

Li YE, Nilot E, Feng X (2020) Observation of guided and reflection P-waves in urban ambient noise cross-correlograms. In: SEG Technical Program Expanded Abstracts 2020, Society of Exploration Geophysicists, pp 2100–2104

Li Z, Lynn W, Chambers R, Larner K, Abma R (1991) Enhancements to prestack frequency-wavenumber (fk) migration. Geophysics 56(1):27–40

Lin FC, Moschetti MP, Ritzwoller MH (2008) Surface wave tomography of the western United States from ambient seismic noise: Rayleigh and Love wave phase velocity maps. Geophysical Journal International 173(1):281–298

Lin FC, Ritzwoller MH, Snieder R (2009) Eikonal tomography: surface wave tomography by phase front tracking across a regional broad-band seismic array. Geophysical Journal International 177(3):1091–1110

Liu Y, Xia J, Cheng F, Xi C, Shen C, Zhou C (2020) Pseudo-linear-array analysis of passive surface waves based on beamforming. Geophysical Journal International pp 640–650, DOI 10.1093/gji/ggaa024

Louie JN (2001) Faster, Better: Shear-Wave Velocity to 100 Meters Depth from Refraction Microtremor Arrays. Bulletin of the Seismological Society of America 91(2):347–364

Luo Y, Xia J, Miller RD, Xu Y, Liu J, Liu Q (2008) Rayleigh-Wave Dispersive Energy Imaging Using a High-Resolution Linear Radon Transform. Pure and Applied Geophysics 165(5):903–922, DOI 10.1007/s00024-008-0338-4

Maraschini M, Ernst F, Foti S, Socco LV (2010) A new misfit function for multimodal inversion of surface waves. Geophysics 75(4):G31–G43, DOI 10.1190/1.3436539

McMechan GA, Yedlin MJ (1981) Analysis of dispersive waves by wave field transformation. Geophysics 46(6):869–874

Mi B, Xia J, Shen C, Wang L (2018) Dispersion energy analysis of rayleigh and love waves in the presence of low-velocity layers in near-surface seismic surveys. Surveys in Geophysics 39(2):271–288

Mi B, Xia J, Bradford JH, Shen C (2020) Estimating near-surface shear-wave-velocity structures via multichannel analysis of rayleigh and love waves: An experiment at the boise hydrogeophysical research site. Surveys in Geophysics 41(2):323–341

Mikesell TD, Gribler G, Xu Z, Haney MM, et al. (2017) High-resolution dispersion images from deblurred masw. In: 2017 SEG International Exposition and Annual Meeting, Society of Exploration Geophysicists

Miller RD, Xia J, Park CB, Ivanov JM (1999) Multichannel analysis of surface waves to map bedrock. The Leading Edge 18(12):1392–1396

Nakahara H (2006) A systematic study of theoretical relations between spatial correlation and Green's function in one-, two- and three-dimensional random scalar wavefields. Geophysical Journal International 167(3):1097–1105, DOI 10.1111/j.1365-246X.2006.03170.x

Nakata N (2020) Pseudo arrivals generated by frequency normalization for seismic interferometry with scattered waves—stationary-phase analysis. In: SEG Technical Program Expanded Abstracts 2020, Society of Exploration Geophysicists, pp 2085–2089

Nakata N, Snieder R, Tsuji T, Larner K, Matsuoka T (2011) Shear wave imaging from traffic noise using seismic interferometry by cross-coherence. Geophysics 76(6):SA97–SA106

Nakata N, Chang JP, Lawrence JF, Boué P (2015) Body wave extraction and tomography at long beach, california, with ambient-noise interferometry. Journal of Geophysical Research: Solid Earth 120(2):1159–1173, DOI 10.1002/2015JB011870

Nakata N, Boué P, Brenguier F, Roux P, Ferrazzini V, Campillo M (2016) Body and surface wave reconstruction from seismic noise correlations between arrays at Piton de la Fournaise volcano. Geophysical Research Letters 43, DOI 10.1002/2015GL066997

Nazarian S, Stokoe II KH, Hudson WR (1983) Use of spectral analysis of surface waves method for determination of moduli and thicknesses of pavement systems. Transportation Research Record (930)

O'Connell DRH, Turner JP (2011) Interferometric Multichannel Analysis of Surface Waves (IMASW). Bulletin of the Seismological Society of America 101(5):2122–2141

Okada H, Suto K (2003) The microtremor survey method. Society of Exploration Geophysicists

Pan Y, Xia J, Xu Y, Gao L, Xu Z (2016a) Love-wave waveform inversion in time domain for shallow shear-wave velocity. Geophysics 81(1):R1–R14, DOI 10.1190/geo2014-0225.1

Pan Y, Xia J, Xu Y, Xu Z, Cheng F, Xu H, Gao L (2016b) Delineating Shallow S - Wave Velocity Structure Using Multiple Ambient-Noise Surface-Wave Methods: An Example from Western Junggar, China. Bulletin of the Seismological Society of America 106(2):327–336, DOI 10.1785/0120150014

Pan Y, Gao L, Bohlen T (2019) High-resolution characterization of near-surface structures by surface-wave inversions: From dispersion curve to full waveform. Surveys in Geophysics 40(2):167–195

Pang J, Cheng F, Shen C, Dai T, Ning L, Zhang K (2019) Automatic passive data selection in time domain for imaging near-surface surface waves. Journal of Applied Geophysics 162:108–117, DOI 10.1016/j.jappgeo.2018.12.018

Park C, Miller R, Laflen D, Neb C, Ivanov J, Bennett B, Huggins R (2004) Imaging dispersion curves of passive surface waves. In: SEG technical program expanded abstracts 2004, Society of Exploration Geophysicists, pp 1357–1360

Park CB, Carnevale M (2010) Optimum masw survey—revisit after a decade of use. In: GeoFlorida 2010: Advances in Analysis, Modeling & Design, pp 1303–1312

Park CB, Miller RD, Xia J (1998) Imaging dispersion curves of surface waves on multi-channel record. In: SEG Technical Program Expanded Abstracts 1998, Society of Exploration Geophysicists, pp 1377–1380

Park CB, Miller RD, Xia J (1999) Multichannel analysis of surface waves. Geophysics 64(3):800–808

Park CB, Miller RD, Ivanov J (2002) Filtering Surface Waves. In: Symposium on the Application of Geophysics to Engineering and Environmental Problems 2002, Environment and Engineering Geophysical Society, Figure 1, pp SEI9–SEI9, DOI 10.4133/1.2927182

Picozzi M, Parolai S, Bindi D (2010) Deblurring of frequency-wavenumber images from small-scale seismic arrays. Geophysical Journal International 181(1):357–368, DOI 10.1111/j.1365-246X.2009.04471.x

Poupinet G, Ellsworth W, Frechet J (1984) Monitoring velocity variations in the crust using earthquake doublets: An application to the calaveras fault, california. Journal of Geophysical Research: Solid Earth 89(B7):5719–5731

Prieto G, Lawrence J, Beroza G (2009) Anelastic Earth structure from the coherency of the ambient seismic field. Journal of Geophysical Research: Solid Earth 114(B7)

Rafaely B, Weiss B, Bachmat E (2007) Spatial aliasing in spherical microphone arrays. IEEE Transactions on Signal Processing 55(3):1003–1010

Ren L, Gao F, Wu Y, Williamson P, Wang W, McMechan GA (2020) Automatic picking of multi-mode dispersion curves using CNN-based machine learning. In: SEG Technical Program Expanded Abstracts 2020, Society of Exploration Geophysicists, pp 1551–1555

Rost S, Thomas C (2002) Array seismology: Methods and applications. Reviews of Geophysics 40(3):1008, DOI 10.1029/2000RG000100

Safani J, O'Neill A, Matsuoka T, Sanada Y (2005) Applications of love wave dispersion for improved shear-wave velocity imaging. Environmental and Engineering Geophysics 10(2):135–150

Schwab F, Knopoff L (1972) Fast surface wave and free mode computations. In: Methods in Computational Physics: Advances in Research and Applications, vol 11, Elsevier, pp 87–180

Shapiro NM, Campillo M (2004) Emergence of broadband rayleigh waves from correlations of the ambient seismic noise. Geophysical Research Letters 31(7)

Snieder R (2004) Extracting the green's function from the correlation of coda waves: A derivation based on stationary phase. Physical Review E 69(4):046610

Snieder R, Miyazawa M, Slob E, Vasconcelos I, Wapenaar K (2009) A Comparison of Strategies for Seismic Interferometry. Surveys in Geophysics 30(4-5):503–523, DOI 10.1007/s10712-009-9069-z

Socco LV, Foti S, Boiero D (2010) Surface-wave analysis for building near-surface velocity models—established approaches and new perspectives. Geophysics 75(5):75A83–75A102

Song YY, Castagna JP, Black RA, Knapp RW (1989) Sensitivity of near-surface shear-wave velocity determination from rayleigh and love waves. In: SEG Technical Program Expanded Abstracts 1989, Society of Exploration Geophysicists, pp 509–512

Stokoe KI, Nazarian S (1983) Effectiveness of ground improvement from spectral analysis of surface waves. In: Proceeding of the eighth European conference on soil mechanics and foundation engineering

Strobbia C, Cassiani G (2011) Refraction microtremors: Data analysis and diagnostics of key hypotheses. Geophysics 76(3), DOI 10.1190/1.3560246

Thorson JR, Claerbout JF (1985) Velocity-stack and slant-stack stochastic inversion. Geophysics 50(12):2727–2741

Tromp J, Luo Y, Hanasoge S, Peter D (2010) Noise cross-correlation sensitivity kernels. Geophysical Journal International 183(2):791–819

Tsai VC, Moschetti MP (2010) An explicit relationship between time-domain noise correlation and spatial autocorrelation (SPAC) results. Geophysical Journal International 182(1):454–460, DOI 10.1111/j.1365-246X.2010.04633.x

Turner G (1990) Aliasing in the tau-p transform and the removal of spatially aliased coherent noise. Geophysics 55(11):1496–1503

Wapenaar K (2004) Retrieving the elastodynamic green's function of an arbitrary inhomogeneous medium by cross correlation. Physical Review Letters 93(25):254301

Wapenaar K, van der Neut J, Ruigrok E, van der Neut J (2008) Passive seismic interferometry by multidimensional deconvolution. Geophysics 73(NO.6):A51—-A56

Wathelet M, Jongmans D, Ohrnberger M (2004) Surface-wave inversion using a direct search algorithm and its application to ambient vibration measurements. Near Surface Geophysics 2(4):211–221

Winsborrow G, Huws D, Muyzert E (2003) Acquisition and inversion of love wave data to measure the lateral variability of geo-acoustic properties of marine sediments. Journal of Applied Geophysics 54(1-2):71–84

Xi C, Mi B, Dai T, Liu Y, Ning L (2020) Spurious signals attenuation using SVD-based Wiener filter for near-surface ambient noise surface wave imaging. Journal of Applied Geophysics 183:104220

Xi C, Xia J, Mi B, Dai T, Liu Y, Ning L (2021) Modified Frequency-Bessel Transform Method for Dispersion Imaging of Rayleigh Waves from Ambient Seismic Noise. DOI 10.1093/gji/ggab008

Xia J, Miller RD, Park CB (1999) Estimation of near-surface shear-wave velocity by inversion of rayleigh waves. Geophysics 64(3):691–700

Xia J, Miller RD, Park CB, Ivanov J (2000) Construction of 2-d vertical shear-wave velocity field by the multichannel analysis of surface wave technique. In: 13th EEGS Symposium on the Application of Geophysics to Engineering and Environmental Problems, European Association of Geoscientists & Engineers, pp cp–200

Xia J, Miller RD, Park CB, Tian G (2003) Inversion of high frequency surface waves with fundamental and higher modes. Journal of Applied Geophysics 52(1):45–57

Xia J, Xu Y, Miller RD (2007) Generating an image of dispersive energy by frequency decomposition and slant stacking. Pure and Applied Geophysics 164(5):941–956

Xia J, Miller RD, Xu Y, Luo Y, Chen C, Liu J, Ivanov J, Zeng C (2009) High-frequency rayleigh-wave method. Journal of Earth Science 20(3):563–579

Xia J, Xu Y, Luo Y, Miller RD, Cakir R, Zeng C (2012) Advantages of Using Multichannel Analysis of Love Waves (MALW) to Estimate Near-Surface Shear-Wave Velocity. Surveys in Geophysics 33(5):841–860, DOI 10.1007/s10712-012-9174-2

Xu Y, Zhang B, Luo Y, Xia J (2013) Surface-wave observations after integrating active and passive source data. The Leading Edge 32(6):634–637

Xu Z, Xia J, Luo Y, Cheng F, Pan Y (2016) Potential misidentification of love-wave phase velocity based on three-component ambient seismic noise. Pure and Applied Geophysics 173(4):1115–1124

Xu Z, Dylan Mikesell T, Xia J, Cheng F (2017) A comprehensive comparison between the refraction microtremor and seismic interferometry methods for phase-velocity estimation. Geophysics 82(6):EN99–EN108

Yan FG, Cao B, Rong JJ, Shen Y, Jin M (2016) Spatial aliasing for efficient direction-of-arrival estimation based on steering vector reconstruction. EURASIP Journal on Advances in Signal Processing 2016(1):1–8

Yang Y, Ritzwoller MH, Levshin AL, Shapiro NM (2007) Ambient noise Rayleigh wave tomography across Europe. Geophysical Journal International 168(1):259–274

Yao H, van der Hilst RD (2009) Analysis of ambient noise energy distribution and phase velocity bias in ambient noise tomography, with application to SE Tibet. Geophysical Journal International 179(2):1113–1132

Yilmaz O (1987) Seismic data processing, society of exploration geophysicists, tulsa

Yin X, Xia J, Shen C, Xu H (2014) Comparative analysis on penetrating depth of high-frequency Rayleigh and Love waves. Journal of Applied Geophysics 111(0):86–94, DOI 10.1016/j.jappgeo.2014.09.022

Zeng C, Xia J, Liang Q, Chen C (2007) Comparative analysis on sensitivities of love and rayleigh waves. In: SEG Technical Program Expanded Abstracts 2007, Society of Exploration Geophysicists, pp 1138–1141

Zhan Z (2019) Distributed Acoustic Sensing Turns Fiber-Optic Cables into Sensitive Seismic Antennas. Seismological Research Letters DOI 10.1785/0220190112

Zhang K, Li H, Wang X, Wang K (2020) Retrieval of shallow S-wave profiles from seismic reflection surveying and traffic-induced noise. Geophysics 85(6):EN105–EN117

Zhou C, Xi C, Pang J, Liu Y (2018) Ambient noise data selection based on the asymmetry of cross-correlation functions for near surface applications. Journal of Applied Geophysics 159:803–813

Zhou HW (2014) Practical seismic data analysis. Cambridge University Press

Layer number	$\mathbf{V_p}(m/s)$	$\mathbf{V_s}(m/s)$	$\boldsymbol{\rho}(g/cm^3)$	$\mathbf{h}(m)$
1	400	800	2.0	10
2	200	400	2.0	10
3	600	1200	2.0	10
Half-space	800	1600	2.0	Infinite

Table 1 Parameters of a four-layer model.

Layer number	$\mathbf{V_p}(m/s)$	$\mathbf{V_s}(m/s)$	$\boldsymbol{\rho}(g/cm^3)$	$\mathbf{h}(m)$
1	200	800	2.0	10
Half-space	400	1200	2.0	Infinite

Table 2 Parameters of a two-layer model.

List of Tables

List of Figures

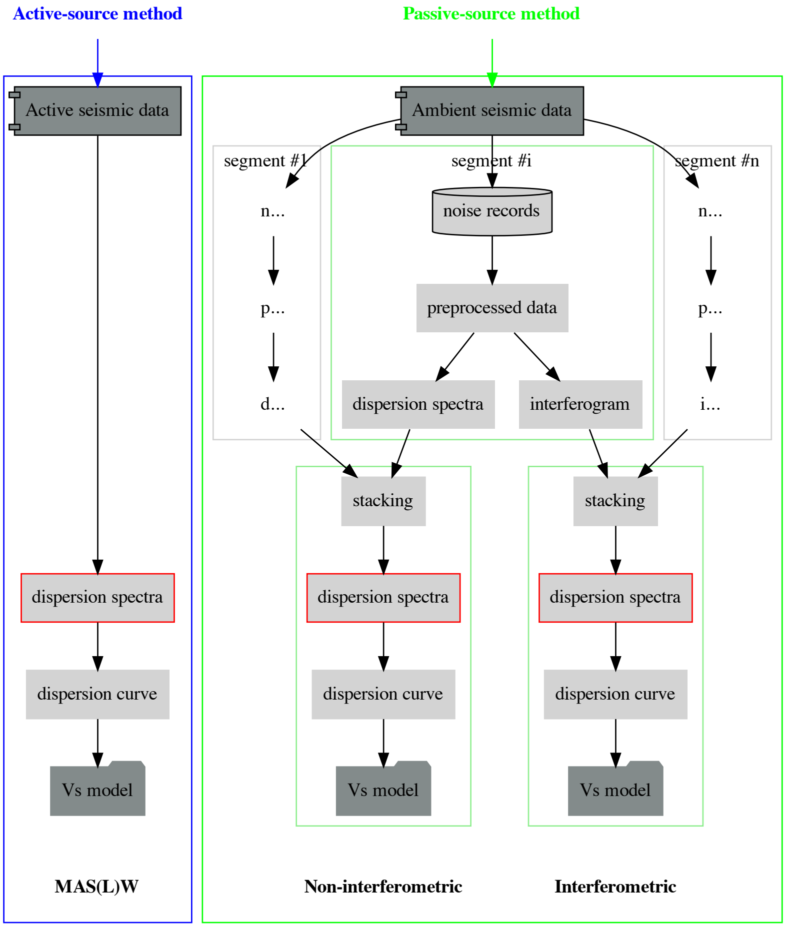

Fig. 1 Flowchart for two types of surface wave methods, the active-source method (the left panel) and the passive-source method (the right panel).

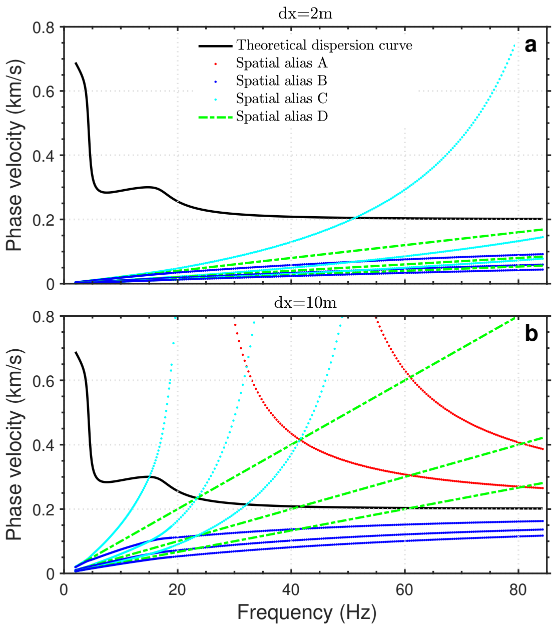

Fig. 2 A comparison of the predicted spatial aliasing with different spatial sampling, $dx = 2m$ (a) and $dx = 10m$ (b). The black curves show the theoretical dispersion curves calculated from a four-layer earth model (Tab.1) by Knopoff's method (Schwab and Knopoff, 1972); four colored dotted curves represent four types of spatial aliasing, A (red, eq.9a), B (blue, eq.9b), C (cyan, eq.9c), D (green, eq.9d), respectively.

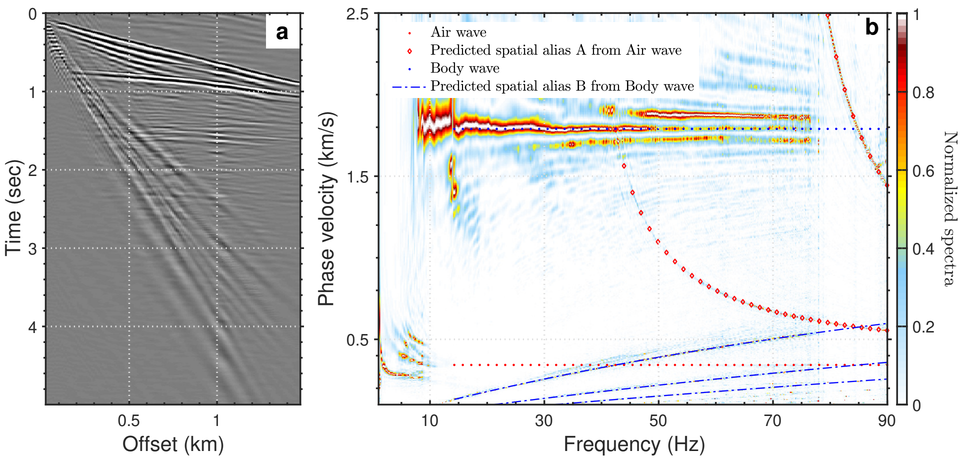

Fig. 3 An example of the type A and B spatial aliasing. a). the observed seismic shot gather; b). the obtained dispersion measurement. The red dotted line indicates the weak air wave energy; the red diamond curves represent the predicted type A spatial aliasing from air wave; the blue dotted line indicates the non-dispersive body wave energy; the blue dash-dot curves represent the predicted type B spatial aliasing.

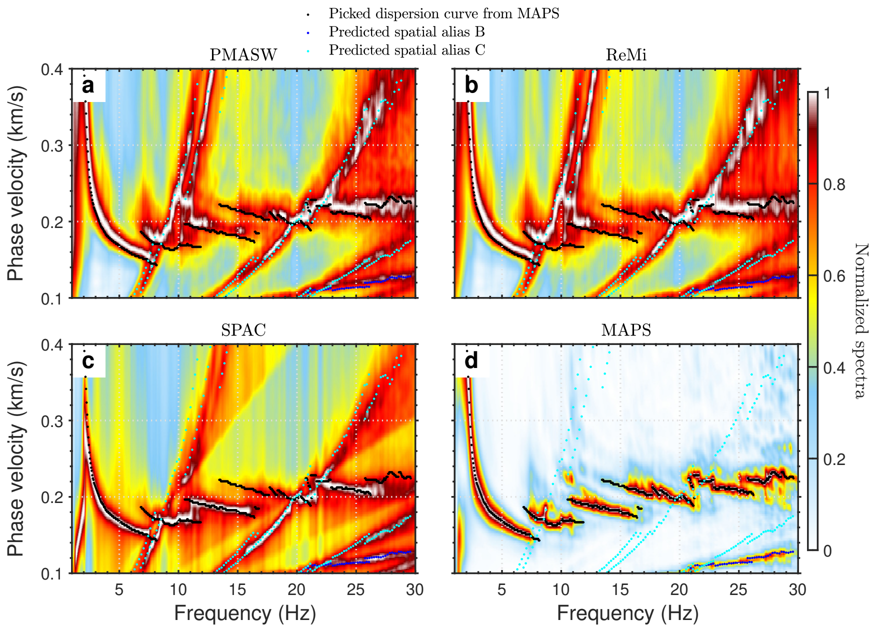

Fig. 4 An example of the type C spatial aliasing. a-d present the obtained dispersion spectra using different passive-source surface wave imaging methods, PMASW, ReMi, SPAC, and MAPS, respectively. The black dotted curves represent the picked dispersion curve from MAPS; the blue dotted curves indicate the predict type B spatial aliasing; the cyan dotted curves indicate the predicted type C spatial aliasing.

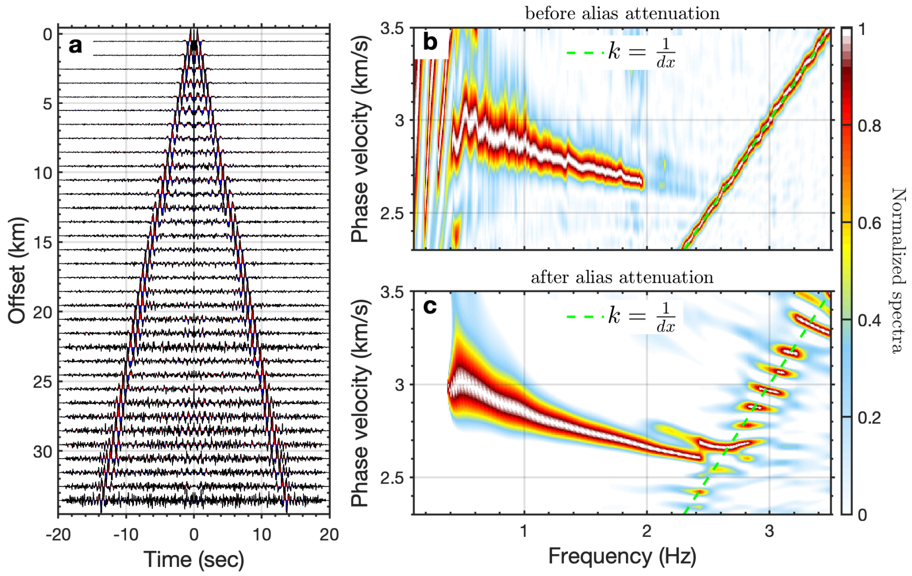

Fig. 5 An example of the type D spatial aliasing. a). the bin-stacked virtual source gather retrieved from ambient noise interferometry; b) and c). the obtained dispersion measurements before and after aliasing attenuated. The green dashed line indicates the predicted spatial aliasing.

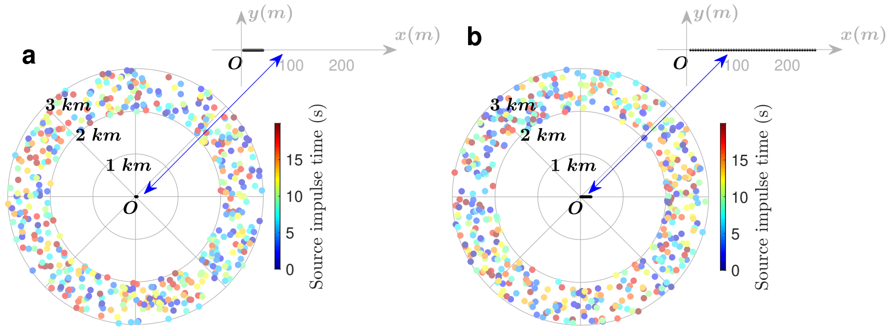

Fig. 6 Random noise sources and receivers configurations for seismic noise modeling with different array length, 50m (a) and 250m (b). The black dots denote the receivers; the face color of the random sources are coded by the random impulse time.

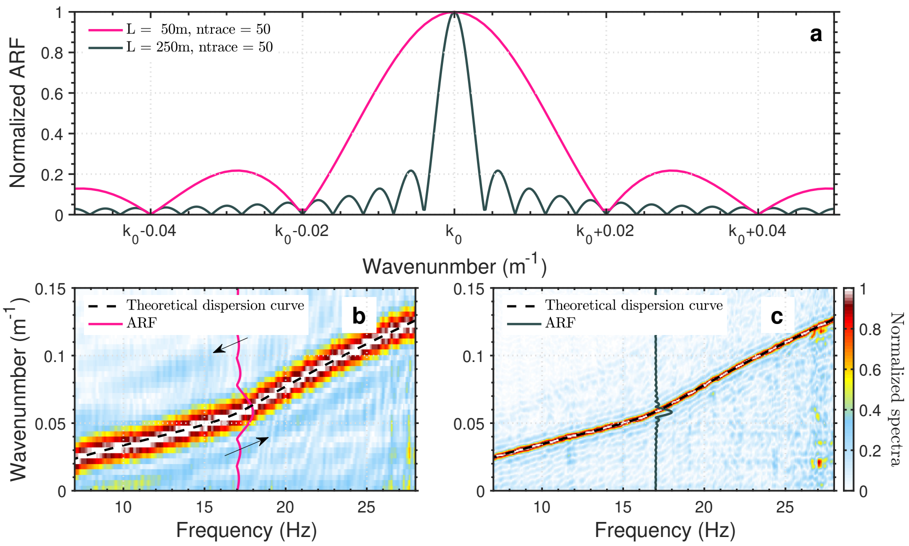

Fig. 7 a) Array response functions for two linear arrays with different array lengths, 50m (the pink line) and 250m (the gray line). b-c present the corresponding dispersion spectra, respectively. The black dashed lines in b and c are the theoretical dispersion curves; two colored, pink and gray, solid lines are the corresponding ARFs at frequency 17 Hz; the black arrows on b indicate the wiggles artifacts from the array response.

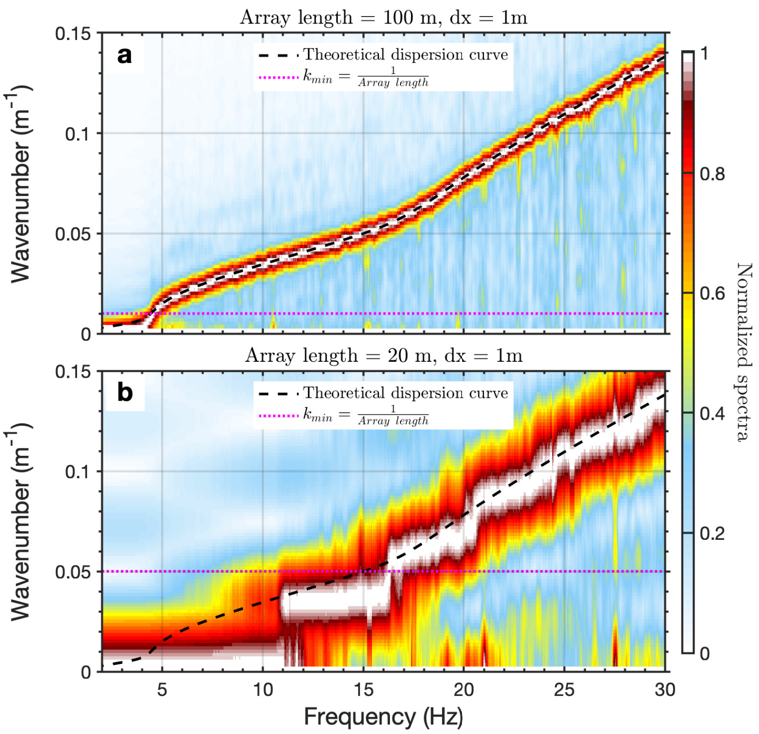

Fig. 8 Effects of array lengths, 100m (a) and 20m (b), on the minimum wavenumber (or the maximum wavelength) for the surface wave dispersion measurement. The pink dashed lines indicate the minimum wavenumber (or the maximum wavelength) inferred from the array length; the black dashed lines represent the theoretical dispersion curve. Note that no data preprocessing procedure is included prior to noise cross-correlation.

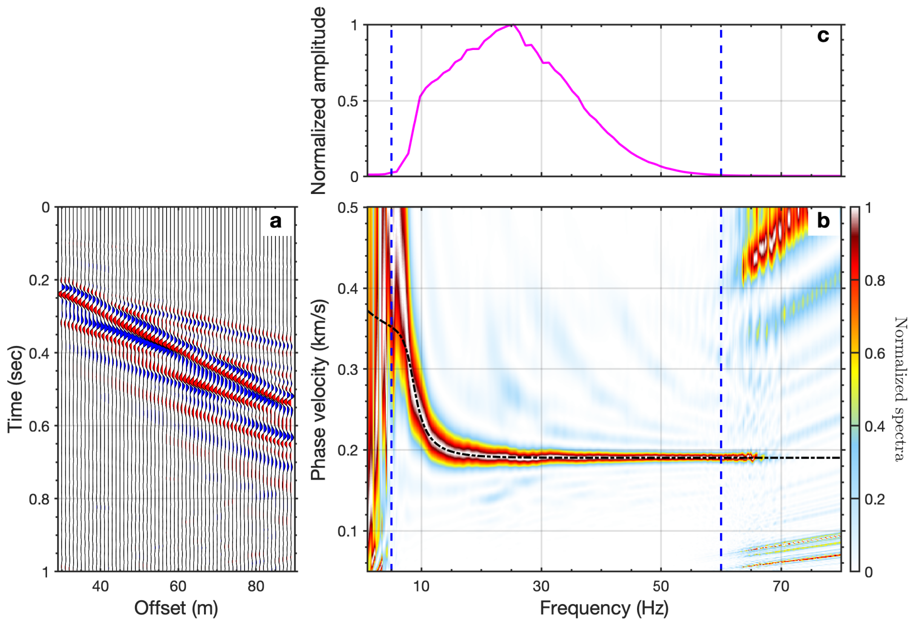

Fig. 9 a). A synthetic active-source surface wave shot gather; b). the obtained dispersion spectra using the phase-shift method; c). the normalized spectrum. The black dashed line on b represents the theoretical dispersion curve; the blue dash lines on b and c indicate the two ends, 5Hz and 65Hz, where the spectrum amplitudes are approaching zero.

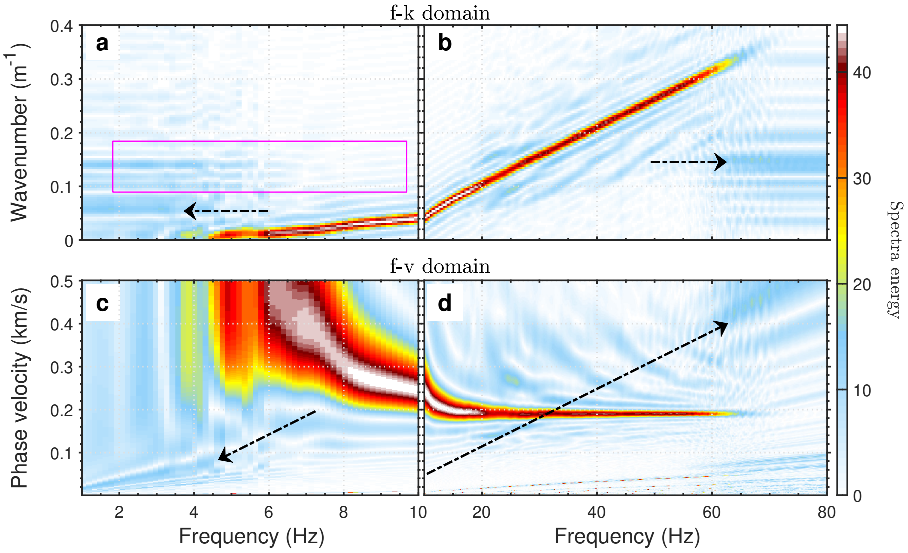

Fig. 10 The obtained dispersion spectra without frequency-direction normalization. a-b present the spectra in $f-k$ domain; c-d present the spectra in $f-v$ domain. The black dashed arrows on a and b indicate the artifacts with constant wavenumber; the black dashed arrows on c and d indicate the radial pattern artifacts; the pink box highlights the consistency between the horizontal artifacts at lower frequency ($<$ 5Hz) and the array response artifacts (wiggles) at the higher frequency ($>$ 5Hz). Note that we break the frequency axis to emphasize the lower frequency band.

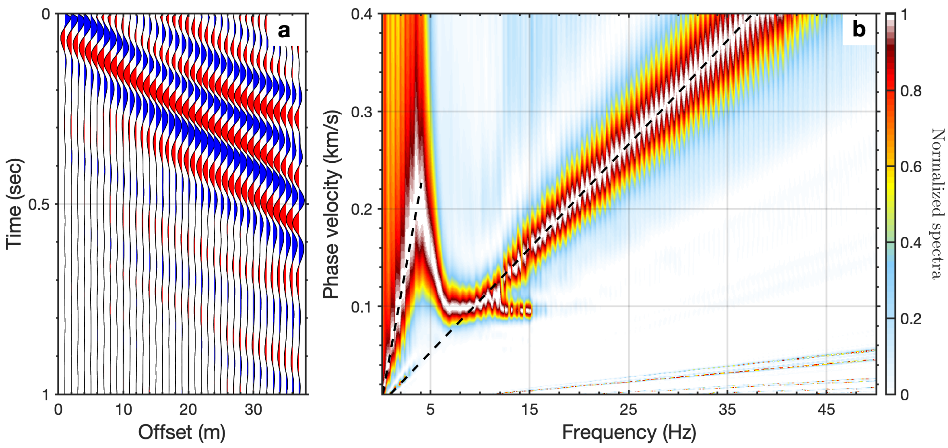

Fig. 11 An example of the radial pattern artifacts for field example #1. a). The bin-stacked virtual source gather retrieved from ambient noise interferometry without noise data preprocessing. The bin-size is 1m. b). Dispersion measurement with distinct artifacts. The black dashed lines highlight the radial pattern artifacts.

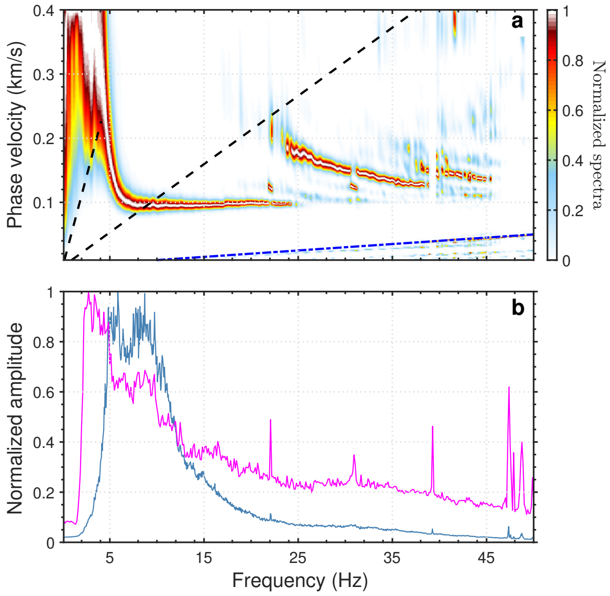

Fig. 12 a). Dispersion spectra with spectral whitening included prior to cross-correlation. The black dashed lines highlight the radial pattern artifacts; the blue dashed line indicates the maximum wavenumber (or the minimum wavelength) inferred from two times of the Nyquist wavenumber ($k_{max} = 2 * \frac{1}{2*dx}$). b). The spectrum of extracted cross-correlations without (the dark blue curve) and with (the pink curve) spectral whitening.

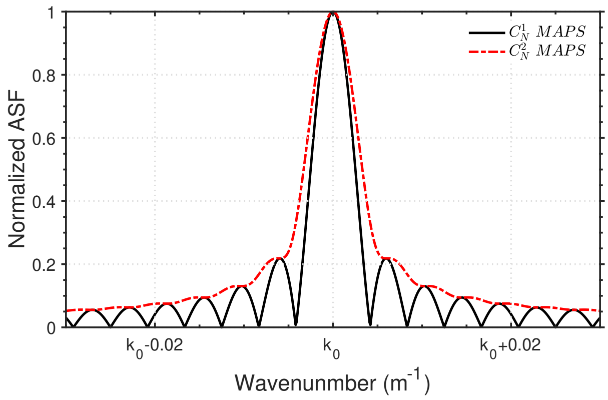

Fig. 13 A comparison of ARFs between one virtual-source gather and multiple virtual-sources gather. Here we take an array of 24 sensors with 10m spatial interval as example.

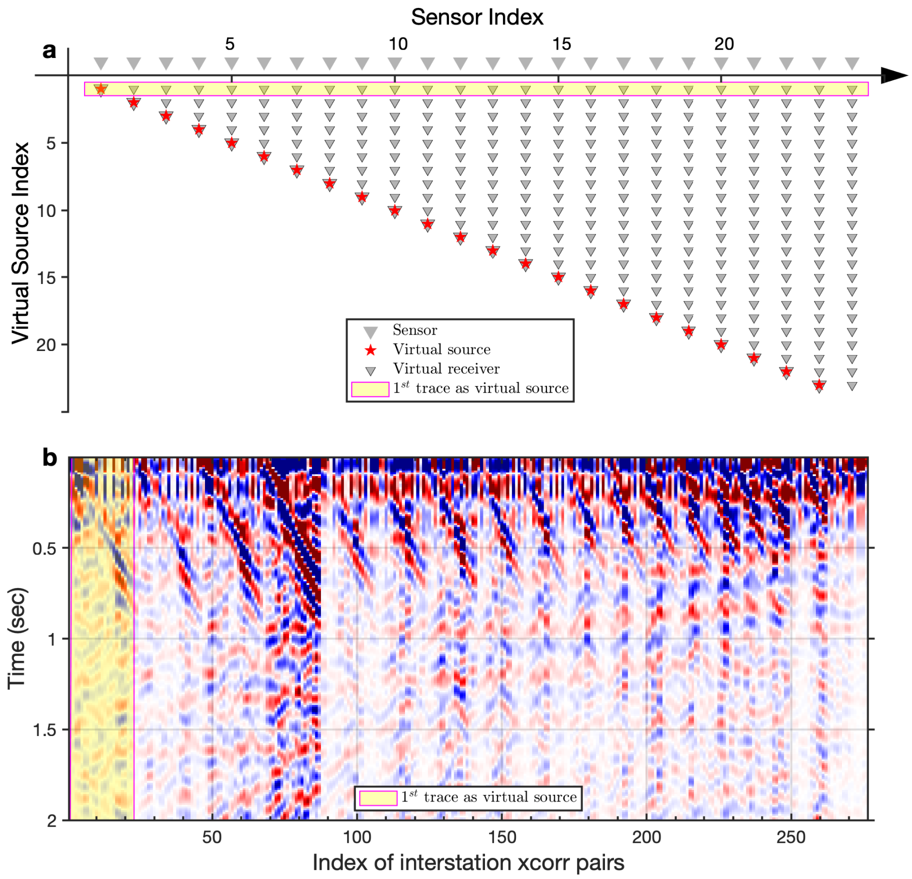

Fig. 14 a). Virtual source and virtual receiver configuration for C_N^2 inter-station cross-correlation pairs. b). The extracted C_N^2 inter-station cross-correlation pairs using ambient noise interferometry. The yellow box highlights the one virtual-source gather with the first trace as the virtual source.

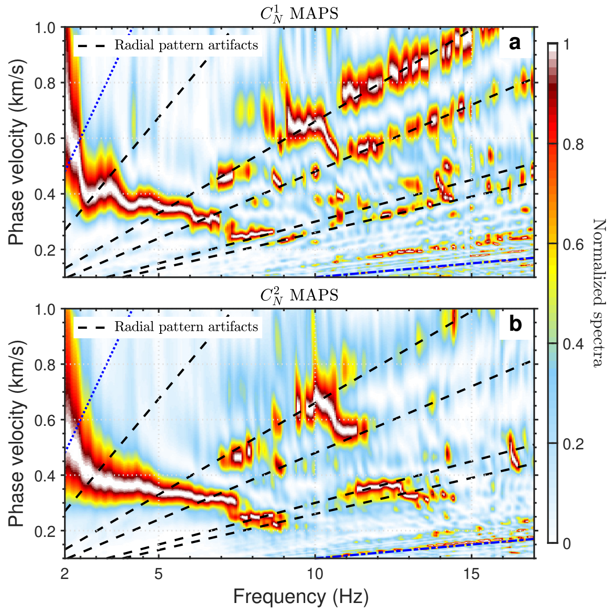

Fig. 15 a). Dispersion spectra of MAPS by using the one virtual-source gather. b). Dispersion spectra of MAPS by using the multiple virtual-sources gather. The black dashed lines indicate the radial pattern artifacts.

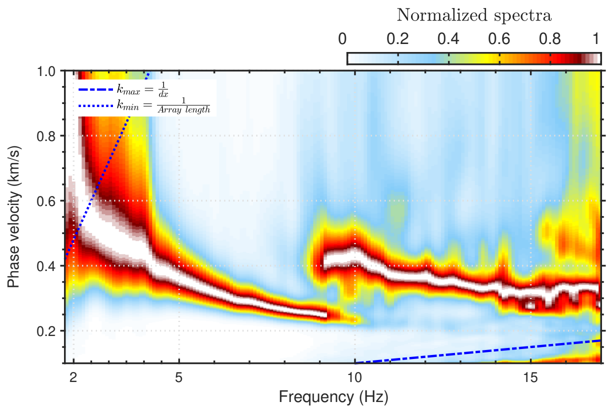

Fig. 16 An example of the radial pattern artifacts attenuation using data-selection technique from Cheng et al. (2019).

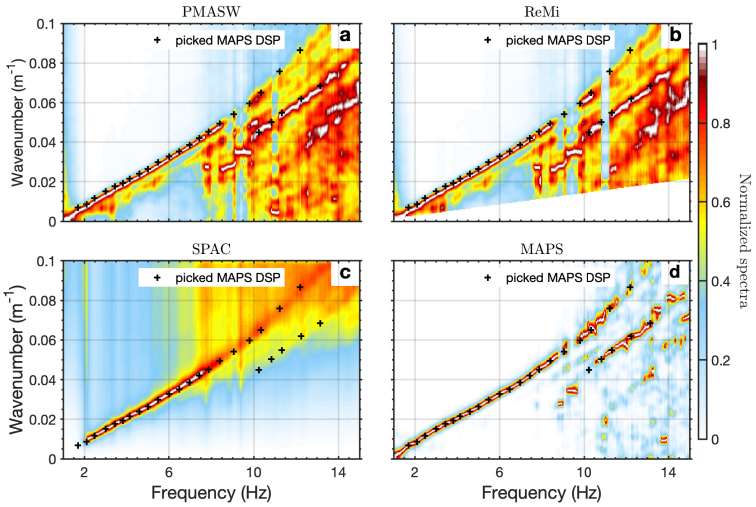

Fig. 17 An example of the artifacts from the non-interferometric methods from Cheng et al. (2020). a-d present the obtained dispersion spectra using different passive-source surface wave imaging methods, PMASW, ReMi, SPAC, and MAPS, respectively.

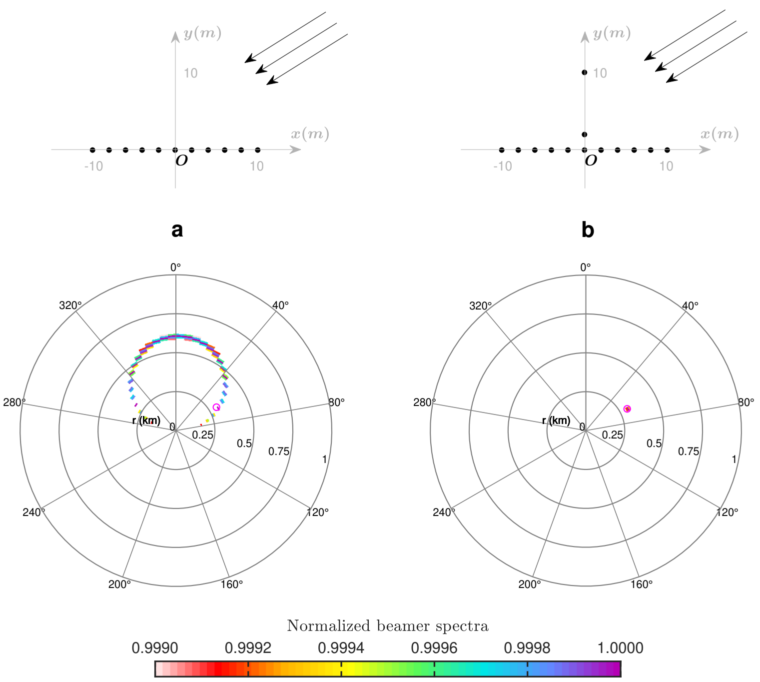

Fig. 18 Array responses for the linear array (a) and the pseudo-linear array (b). The black dots denote the receivers; the black arrows indicate the plane wave; the pink circles indicate the target azimuth and velocity solution.